SEARS
Ship Emissions to Atmosphere Reporting Service
Contract No. 400104295

D2 – Prototype NO_x product development

Reference:
SEARS_D2_NOx_product_development
Issue 1.0
Date: December 2014

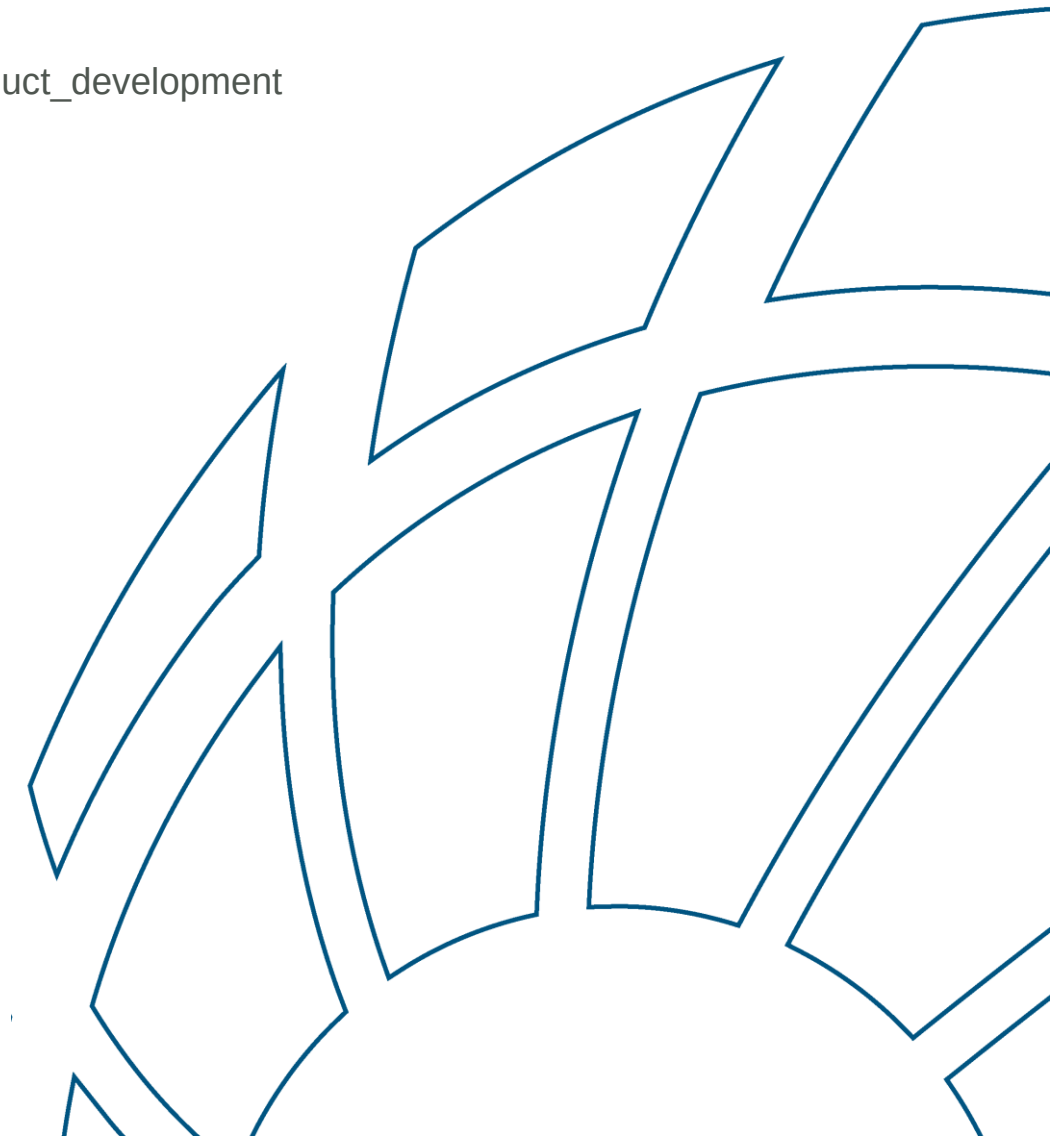

Document status sheet

Title	D2 – Prototype NO_x product development
Code	SEARS-D2
Date	December 2014
Status	Final
Issue	1.0
Contractnr	4000104295/11/I-NB
Projectnr	A11025
Project name	SEARS
Prepared for	ESA
Author(s)	Andreas Richter (IUP-UB) Huan Yu (BIRA) Michel van Roozendael (BIRA) Isabelle de Smedt (BIRA) Gerard Hesselmans (HERMESS)
Approved by	: Shane Amaratunga (BMT ARGOSS)
Distribution	: ESA EMSA BMT ARGOSS IUP BIRA HERMESS

Contents

List of abbreviations and acronyms

BIRA	Belgian Institute for Space Aeronomy
CTM	Chemistry-Transport Model
DOAS	Differential Optical Absorption Spectroscopy
ECMWF	European Centres for Medium-range Weather Forecasts
GOME-2	Global Ozone Monitoring Experiment-2
IUP	Institute of Environmental Physics (University of Bremen)
KNMI	Dutch Royal Meteorological Institute
LER	Lambertian Equivalent Reflectance
OMI	Ozone Monitoring Instrument
RTM	Radiative Transfer Model
S4	Sentinel-4
S5P	Sentinel-5 Precursor
SCD	Slant Column Density
TEMIS	Tropospheric Emission Internet Service
TROPOMI	TROPOspheric Monitoring Instrument
VCD	Vertical Column Density
SZA	Solar Zenith Angle
VZA	Viewing Zenith Angle
SAA	Solar Azimuth Angle
VAA	Viewing Azimuth Angle
RAA	Relative Azimuth Angle
COT	Cloud Optical Thickness
CF	Cloud Fraction
CP	Cloud Pressure
MODIS	Moderate Resolution Imaging Spectroradiometer
SNR	Signal-to-noise ratio
MS	Mediterranean Sea
STD	STandard Deviation
EMS	East Mediterranean Sea
GMES	Global Monitoring of the Environment and Security
SA	Surface Albedo

1. Introduction

1.1. State of the art

1.1.1. Satellite detection of shipping NO_2

The importance of ship emissions for the marine boundary layer has been recognised some time ago. One of the key species emitted is NO_x, the sum of NO and NO_2. The Global Ozone Monitoring Experiment (GOME), launched in 1995 provided the first global view of tropospheric NO_2. However, only nine years later, Beirle et al. (2004) realised that NO_2 from ships can actually be seen in global maps derived from GOME data. They detected a line of NO_2 from India to Indonesia that matched the position of ship tracks. No other ship tracks could be detected, mainly due to the very large pixel size of GOME (320 x 40 km^2). At about the same time, more NO_2 from ship tracks were found in data from the SCIAMACHY (SCanning Imaging Absorption spectroMeter for Atmospheric CartograpHY) instrument launched on ENVISAT in 2002 (Richter et al., 2004). These data have better spatial resolution (60 x 30 km^2), enabling the detection of shipping NO_2 also in the Red Sea, the Persian Gulf and from Indonesia towards Japan and China.

The OMI instrument, launched in 2004, has even better spatial resolution and much better coverage, and additional NO_2 from ships has been observed in the Mediterranean in OMI data (Marmer et al., 2009). Subsequent studies using OMI data and improved filtering techniques enabled the detection and quantification of shipping NO_2 in the bay of Biscay, The North Sea and the Baltic Sea (Vinken et al., 2014) and an additional ship track in the Baltic sea was reported by Ialongo et al., 2014), again from OMI data. The latest UV/visible instrument providing NO_2 data is the GOME-2, launched on Metop-A in October 2006 and on Metop-B in September 2012, and although it has reduced spatial resolution (80 x 40 km^2), the good signal-to-noise ratio of these data resulted in detection of NO_2 from shipping from Europe, around Africa towards Indonesia (Richter et al., 2011). Franke et al, 2009 investigated the temporal evolution of the NO_2 signal from India to Indonesia using data from all available instruments, finding large seasonality, an upward trend, and also interannual variability. A closer look on the temporal evolution of shipping NO_2 and the link to international trading volume was presented in de Ruyter de Wildt (2012), highlighting the reduction in shipping NO_2 signal during the 2008 crisis visible in several shipping lanes observed by GOME-2, OMI and SCIAMACHY. In all cases, averages over one month or longer were used to achieve appropriate signal-to-noise ratios.

1.1.2. Satellite detection of other shipping emissions

Additional signals attributed to ship emissions were reported by Marbach et al., 2009 who detected an enhancement in HCHO in the area where also NO_2 is enhanced between India and Indonesia. The distribution is somewhat more extended spatially, probably because of secondary formation and longer atmospheric lifetime of HCHO. However, the signal is also more difficult to detect and no other HCHO enhancements have been reported in the literature so far. Detection of SO_2 is complicated by the low penetration depth of photons in the UV where SO_2 is retrieved, but under favourable conditions, SO_2 from shipping can be detected (Theys et al., 2014).

1.1.3. Conversion of NO_2 columns to NOx emissions

While satellite observations can provide the NO_2 columns linked to shipping emissions, the quantity of interest often is the emission of NOx itself. As the link between emissions and NO_2 column is complex (it depends on photochemistry, dynamics, observation sensitivity and other parameters), it often involves the use of atmospheric chemistry transport models and explicit inversion techniques.

The first publications on ship emissions (Beirle et al., 2004 and Richter et al., 2004) relied on a direct conversion between NO_2 columns and NOx emission by using a simple lifetime. In Richter et al. (2004), this lifetime was estimated from back of the envelope calculations while Beirle et al. (2004) used the observations of the plume displacement under different wind conditions to estimate NOx lifetime from the satellite data themselves. A much more complex approach using a modified version of the GEOS-chem model having a plume in grid representation of ship emissions was presented by Vinken et al (2014), and can be considered as state of the art today. However, this method is computational expensive and was applied to long-term averages in order to achieve sufficient signal to noise ratio. Therefore, we here evaluate a much simpler approach aiming at rapid updating of existing emission inventories.

2. Satellite NO_2 retrievals used

2.1. TEMIS retrieval

The retrievals of the tropospheric NO_2 columns from TEMIS (van der A et al., 2008) are based on the same basic algorithm for the GOME-2 ($TM4NO_2A$ products version 2.0) and OMI (DOMINO products version 2.) sensors (Boersma et al., 2004, 2007, 2011). This algorithm consists of three steps: (1) using the Differential Optical Absorption Spectroscopy (DOAS) approach to obtain NO_2 slant columns from the satellite-measured reflectance spectrum; (2) separating the stratospheric and tropospheric contribution to the slant column by using a data assimilation technique; and (3) applying a tropospheric air mass factor (AMF) to convert the residual tropospheric slant column to a vertical column. These principles of the retrievals of tropospheric NO_2 from satellite nadir observations published in previous studies are generally the same. Compared with the previous version, the current TEMIS products (Boersma et al., 2011) improved several aspects on the calculation of AMF, such as radiative transfer calculations, terrain heights, surface albedo and the use of an updated CTM. These products have been evaluated in comparison to several independent measurements (Irie et al., 2012; Ma et al., 2013; Lin et al., 2014), and results show generally good correlation but with varying biases. Lin (2014) found that the NO_2 retrieval based on pixel-specific radiative transfer calculations shows better agreement compared with the DOMINO retrieval. However, we found that the difference is mainly due to an issue with the geometry definition in the TEMIS retrieval, leading to a 5-20% bias in NO_2 retrievals between the west and east parts of the satellite swath. Furthermore, a large discrepancy is also found between TEMIS GOME-2 and OMI NO_2 products (Yu et al., 2013), which is inconsistent with the diurnal variation of NO_2 from ground-based measurements, and this difference is ascribed to the diurnal variation of NO_2 profile shapes taken from the TM4 CTM. In this work, we therefore created a new LUT based on the LIDORT v3.6 RTM to calculate altitude dependent box-AMFs, and the use of IMAGESv2 CTM (daily) output at 9:30 and 13:30 as a priori NO_2 profile for the calculation of tropospheric AMF. These AMFs will be used instead of the one provided in the TEMIS product.

2.2. IUP-BREMEN retrieval

Richter et al. (2011) improved the GOME-2 NO_2 retrieval by extending the fitting window used in the DOAS method from the standard 425-450nm to 425-497nm to include more spectral points in the fit, resulting in a reduced scatter of the NO_2 SCDs. Furthermore, an explicit spike removal algorithm was implemented, and this approach significantly reduces the noise for the data in the region of the Southern Atlantic Anomaly. This data set has the potential to improve the detection limit for NO_2 from ships and is therefore also included in this study. The other steps of the retrieval (stratospheric correction and AMF) will be the same as applied for the TEMIS product.

3. Improvements of NO_2 products

3.1. Improved NO_2 SCD retrieval

The improved GOME-2 slant column retrieval reduces the scatter of the NO_2 SCDs by about 25% (Richter et al., 2011). As shown in Figure 3.4 the GOME-2 retrieval using the improved SCDs has less noise than the retrieval with the TEMIS SCDs. At the same time, the shipping NO_2 signals from the improved retrieval are slightly smaller than from the TEMIS NO_2 (Figure 3.7). This difference is the result of the wavelength dependence of surface albedo. Based on the OMI database (Kleipool et al., 2008), the surface albedo at 440nm which represents the centre of fitting windows for the TEMIS products is about 0.047 over the Indian Ocean, while the average albedo is only 0.042 at 461nm corresponding to the fitting window of IUP retrieval. This difference needs to be taken into account for quantitative comparisons.

3.2. Effect of the spatial resolution of a priori NO_2 profiles

NO_2 retrieval from satellite observations is limited by the coarse resolution of the a priori data used for the calculation of the AMF (Heckel et al., 2011), in particular for the NO_2 profile shape, which is important for the detection of the NO_x signals from the ship emission over the narrow shipping lanes. As shown in Figure 3.1, the width of the shipping lane is up to a few tens of kilometres in the CHIMERE model, and the spatial resolution of the global IMAGES/TM4 CTM, which is used in our satellite NO_2 retrieval, is 2°×2.5°/2°×3°, corresponding to hundreds of kilometres. The corresponding AMFs using CHIMERE output display a sharp gradient from the intensive shipping lane towards the ocean background (increasing by 30%-40%), while the patterns with IMAGES/TM4 profiles show a smooth gradient over the shipping track and almost no difference within 1° of latitude around ship lane. NO_2 retrievals using NO_2 profile shapes simulated with the high resolution CTM will be enhanced by 50%-100% for the shipping NO_2 (Figure 3.7).On the other hand, satellite observed NO_2 (slant) columns reduce the shipping NO_2 signal from the narrow ship lanes by 33%-50%.

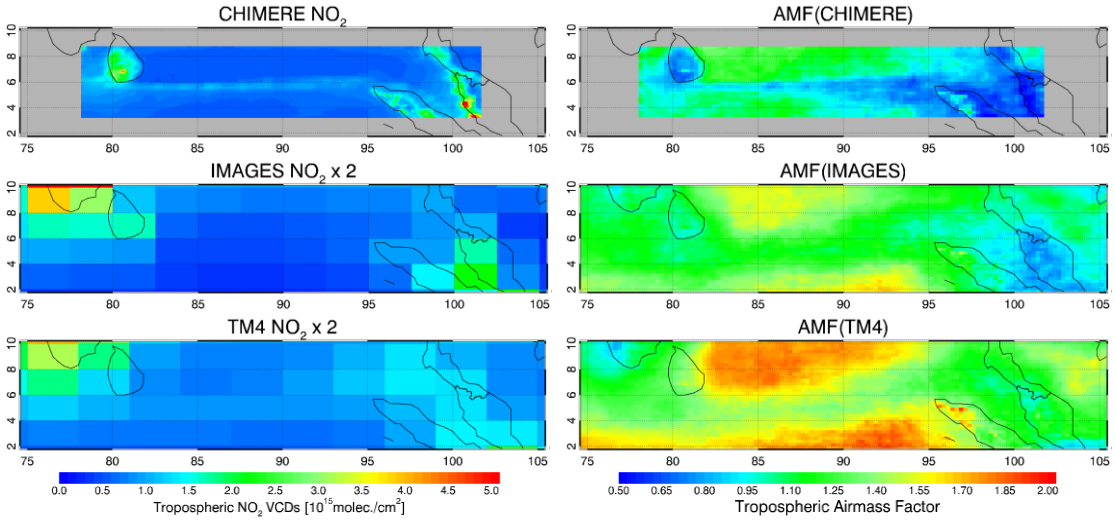

Figure 3.1 Comparisons of modelled NO_2 (left) and NO_2 AMF (right) using the corresponding CTM profiles for OMI observation for March 2007. First row: CHIMERE; second row: IMAGES; third row: TM4. Note that the NO_2 values for IMAGES and TM4 are doubled to enhance NO_2 signal over ocean.

3.3. Gridding

The gridding algorithm for the tropospheric NO_2 data used in this work is divided into two steps (Figure 3.2): (1) First, NO_2 Level 2 data are gridded on a fine grid with a resolution which is several times smaller than the resolution of the target grid (so-called sub-grid). Such as Figure 3.2, the size of the target grid is 0.2°, and NO_2 data is gridded on 0.025° (=0.2°/8), where the value in each sub-grid is the average of all satellite observations intersecting this cell. (2) The value for the target grid is then the average for all the sub-grids in the grid. The obtained result is similar to the area weighted mean of the overlapping pixels. The NO_2 maps produced using this gridding method can well represent the satellite observations at any spatial resolution (Figure 3.3).

As shown in Figure 3.4, the monthly average of tropospheric NO_2 columns from both GOME-2 and OMI observations clearly show the enhanced shipping signal over the Indian Ocean, and the noise level is less than 0.1×10^{15} molec./cm^2, OMI showing slightly larger noise than GOME-2. When decreasing the resolution of the grid, the noise will decrease, but the shipping signal is diluted as well. The shape of the shipping signal strongly depends on the resolution of the grid for GOME-2, and the shipping signal still improves when the resolution of the grid (0.25°×0.25°) is smaller than the resolution of the GOME-2 pixels. The effect is very small for OMI data since the size of both the grid boxes and the OMI pixels is much smaller than the extension of shipping NO_2 signals over this area. At the same time, a coarser grid helps to improve the signal-to-noise ratio.

The results show, that it is very important to use a suitable grid size to optimise the signal-to-noise ratio of NO_2 maps and the shipping signals, in particular for the detection of shipping NO_2 over difficult places, such as over Europe.

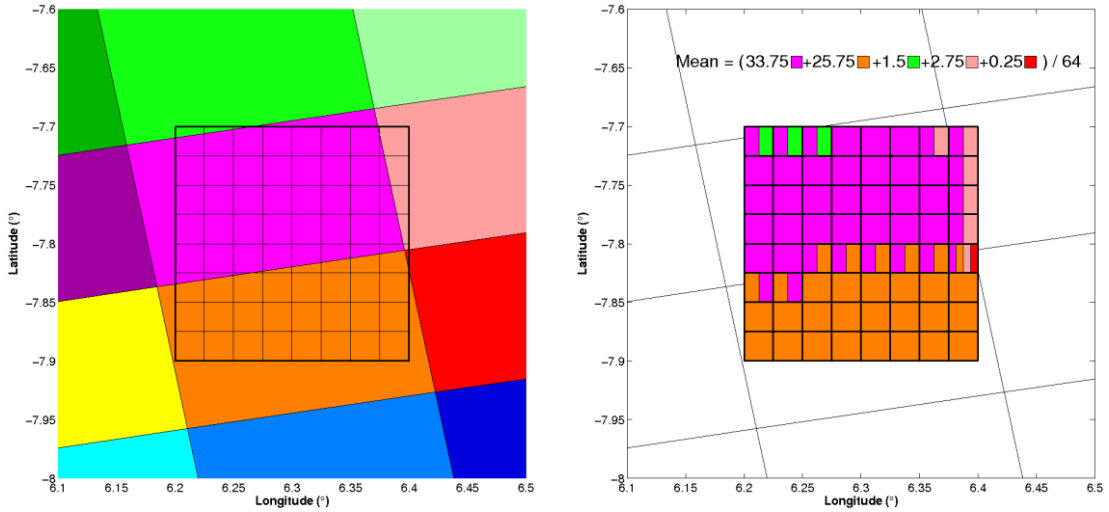

Figure 3.2 Principle of the new gridding algorithm. Left panel: Example of OMI observation, each color represents an individual OMI pixel, the black thick line is a target grid cell. The First step is to split the grid into small subgrid cells (here 8×8), and the value for each subgrid call is the average of all pixels intersecting the cell (right panel). the value for the target grid cell is the average of all sub-grid cells.

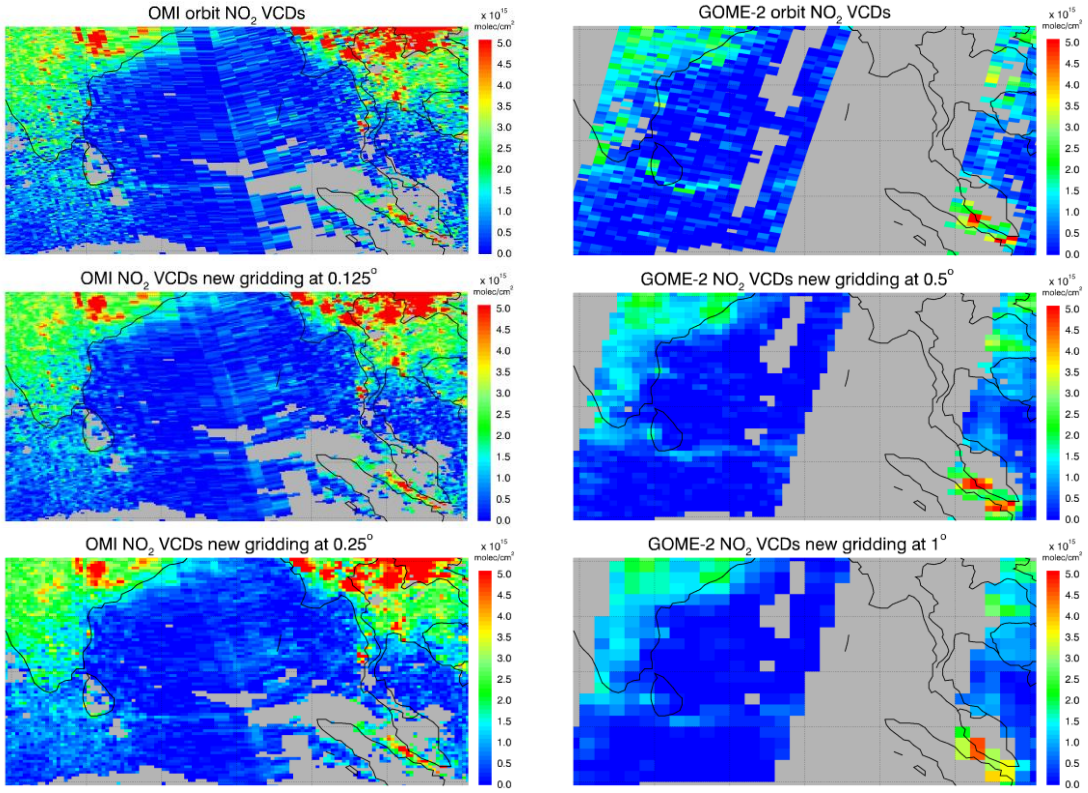

Figure 3.3 Tropospheric NO_2 VCDs (TEMIS retrieval) over the Indian Ocean region from OMI (first column) and GOME-2 (second column) observations for 31, March 2007. Pixels with cloud fraction larger than 30% are excluded. First row: original orbit data; second and third row: gridded data at 0.125°/0.25° for OMI and 0.5°/1° for GOME-2 using the new gridding algorithm.

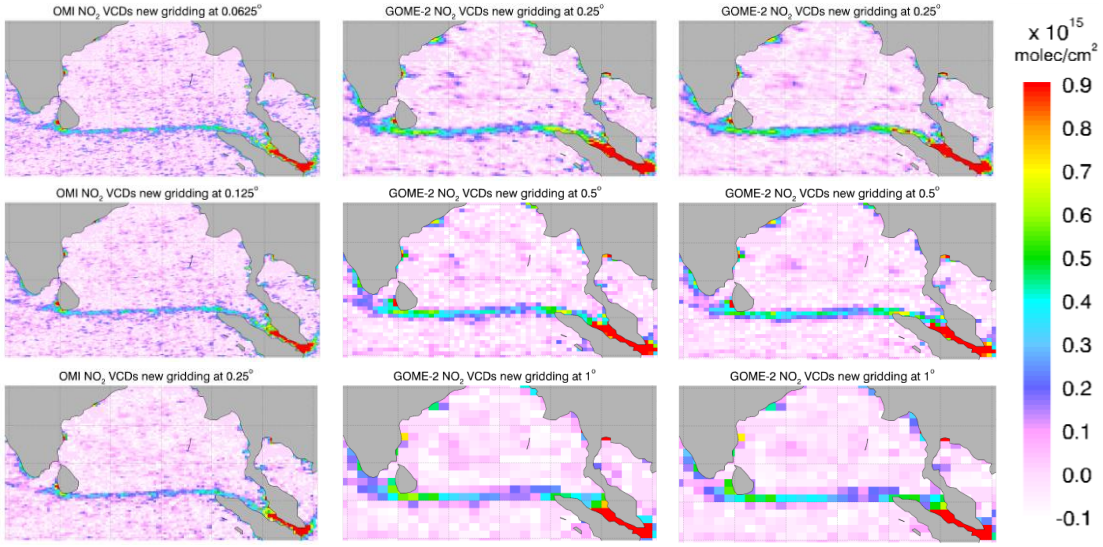

Figure 3.4 Monthly average of tropospheric NO_2 columns derived from the satellite retrievals with different resolution for March 2007. Data have been spatially high pass filtered to highlight the signals from ship emissions. Left panel: OMI TEMIS retrieval; middle panel: GOME-2 TEMIS retrieval; right panel: GOME-2 TEMIS retrieval with improved SCD from IUP. Rows 1-3 represent the monthly data gridded at different spatial resolution (0.0625°/0.125°/0.25° for OMI and 0.25°/0.5°/1.0° for GOME-2).

3.4. Evaluation of CHIMERE and satellite NO_2 VCDs

To compare CHIMERE predicted tropospheric NO_2 columns (Figure 3.1) with the satellite-observed columns (Figure 3.3) for both GOME-2 and OMI, the model data need to be interpolated and regridded to satellite resolution. Therefore, Tropospheric NO_2 VCDs shown in Figure 3.5 are derived by vertically integrating the NO_2 profiles (surface−7km) from the high resolution CHIMERE CTM output, degrading the resolution to GOME-2 and OMI pixel size, interpolating to the corresponding overpass time, and then gridding and averaging them over three months with a horizontal resolution of 0.25º.

Model and OMI measurements show very similar seasonal patterns, but CHIMERE predicted NO_2 columns in the morning are systematically higher than those observed by GOME-2. This discrepancy is arguably due to the differences of the free tropospheric NO_2 simulation between CHIMERE and TM4 CTM, since the tropospheric NO_2 information is mainly coming from the TM4 simulation in the TEMIS NO_2 products over the background areas as result of the assimilation scheme used for the stratospheric correction.

In order to better understand the difference of the shipping signals between model and measurements, we integrate the NO_2 data along the ship track to create a cross-section for each case in each season. The results are shown in Figure 3.7, showing that the shipping signal from GOME-2 is 10%-30% higher than that of OMI. GOME-2 measurements show maxima in winter and minima in summer for shipping NO_2, with about 28% difference between the two seasons. OMI measurements show similar seasonal variation but with a smaller amplitude. The model predicted NO_2 columns have a similar seasonal variation, but the amplitude of change (54% in the morning; 31% in the afternoon) is larger than for satellite observations. The difference of the shipping NO_2 between CHIMERE and satellite observations is up to a factor of 2 (TEMIS+CHIMERE profile versus CHIMERE in Figure 3.7), modelled data being smaller, and largest difference being observed in summer. Moreover, there is a shift of 0.2°-0.3° in the position of the shipping lane between satellite observations and model simulations, which can be linked to the relatively low spatial resolution (0.5°) of the emission inventory used in these simulations. This difference creates also ambiguity in the AMF based on CHIMERE profiles which has a large impact on the results but can introduce problems if the location of the ship track in the model does not fit perfectly with the real ship track (see Mar–Apr–May plot in Figure 3.7).

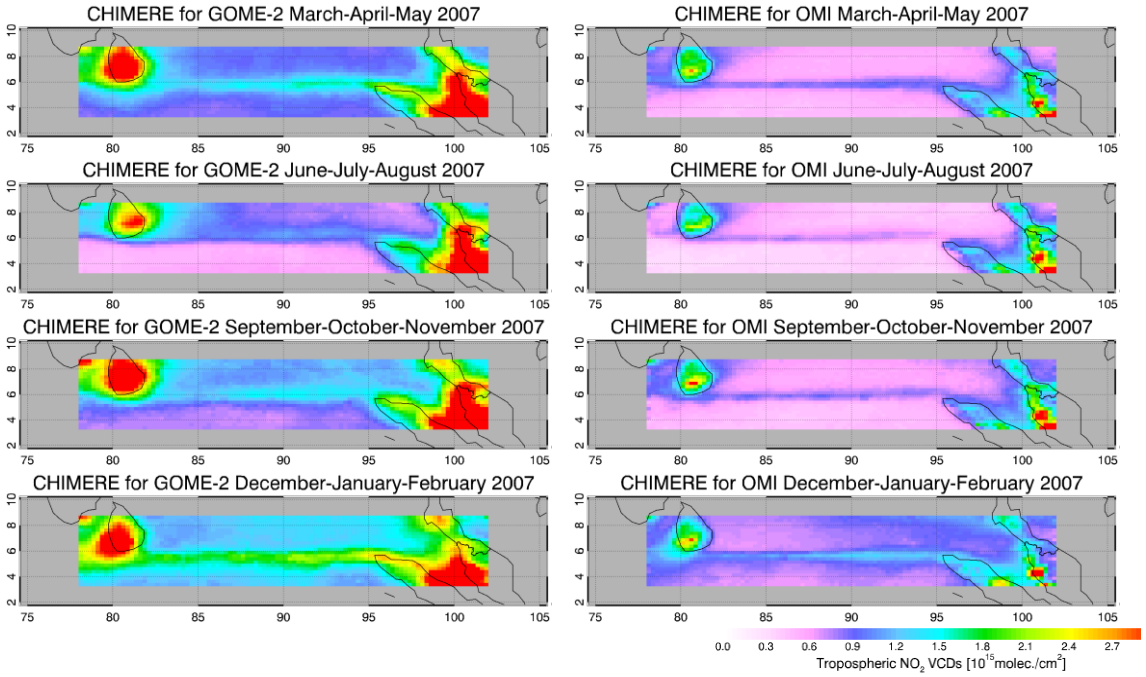

Figure 3.5 Seasonal averages of NO_2 VCDs from CHIMERE simulated for satellite observations (Left: GOME-2; right: OMI)

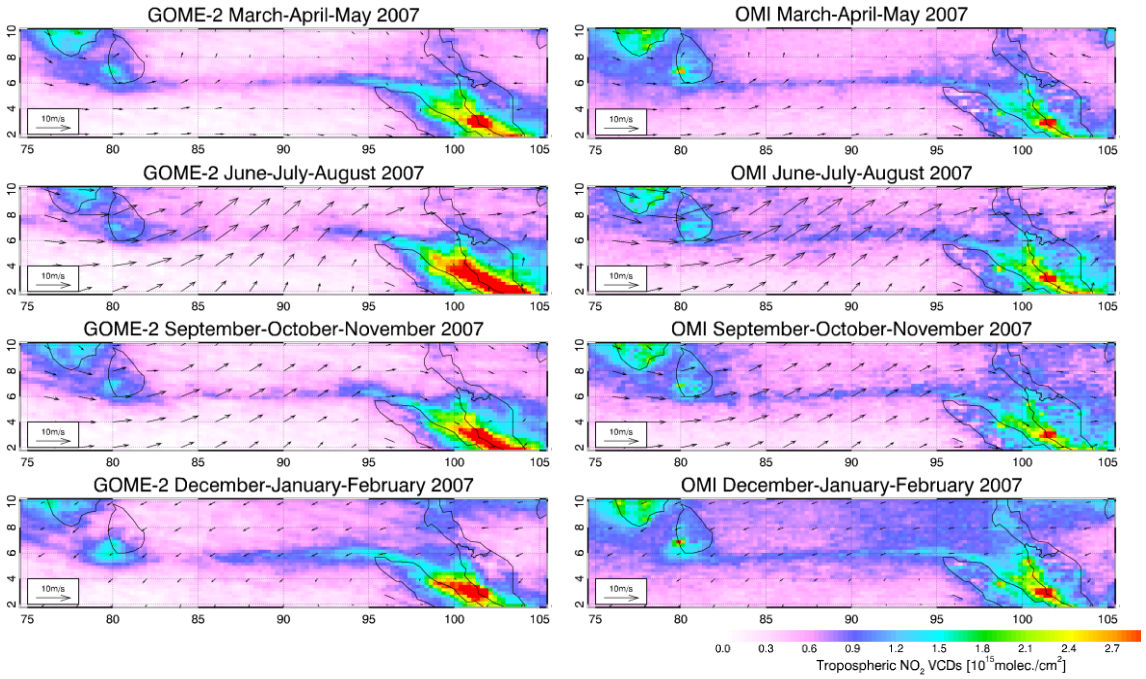

Figure 3.6 Seasonal averages of tropospheric NO_2 VCDs from satellite observations and wind fields for 2007 (Left: GOME-2; Right: OMI). Pixels with cloud fraction above 0.3 are excluded to reduce the retrieval errors, and wind fields are linearly interpolated from ECMWF 6-hour reanalysis data.

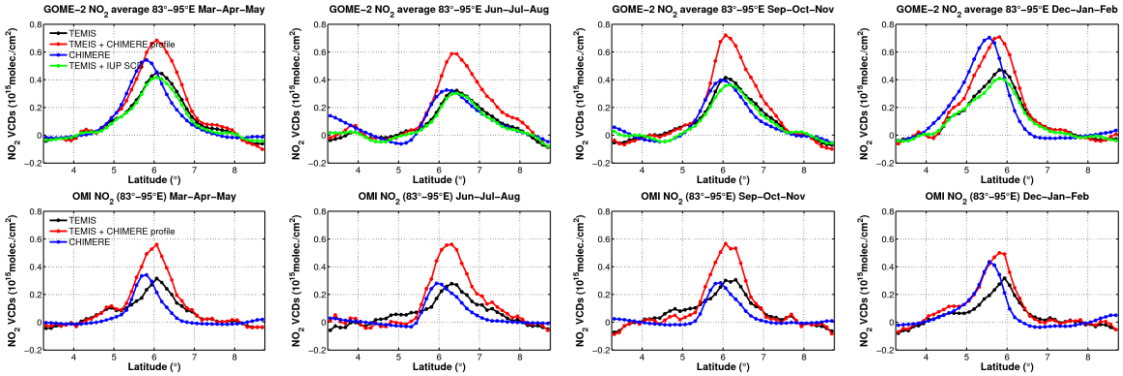

Figure 3.7 Comparison of seasonal along-ship-track averages of tropospheric NO_2 columns over the Indian Ocean between observed columns from GOME-2(upper)/OMI (bottom) and CHIMERE simulations. The area is averaged over longitude (83°–95°E), and a linear background fit is subtracted from the averages.

3.5. Shipping NO_2 over European water

3.5.1. NO_2 VCDs map from Satellite observations

The NO_2 retrieval from GOME-2 and OMI used in this study is similar to the TEMIS retrieval described in section 2.1, except for the cloud correction and surface albedo. We excluded cloudy situations by filtering pixels with cloud fraction above 0.3, in order to limit retrieval errors. There is no cloud correction in the calculation of the AMF for partially cloudy scenes, in order to reduce inconsistencies related to discrepancies in the cloud products. Surface albedo is taken from the same dataset (OMI dataset, Kleipool et al., 2008) for both instruments to further reduce the inconsistency between GOME-2 and OMI retrieval. Figure 3.8 (top panel) shows multiannual averages of tropospheric NO_2 columns observed by GOME-2 (2007-2010) and OMI (2005-2010) over Europe on a horizontal grid of 0.25°×0.25° for GOME-2 and 0.125°×0.125° for OMI Figure 3.8

In order to obtain clearer shipping signals, a spatial high pass filter is applied as shown in the bottom panel of Figure 3.8. This approach is similar to the method described in Richter et al., 2011, using a moving average (1°(lat)x2°(lon) for OMI and 1.875°x3.75° for GOME-2) to smooth the NO_2 field, and then subtracting the smoothed field from the average. In order to reduce the impact of shipping lanes on the background map, in the residual high values (> 0.1×10^{15}) are masked, and then the above procedure is repeated once to determine the NO_2 hotspots. Finally, the hotspots are masked, the field is smoothed, and the smoothed field is subtracted from the average map. From the figures, the following conclusions can be drawn:

- NO_2 columns observed from OMI and GOME-2 show good agreement.
  NO_2 hotspots are more obvious in OMI than in GOME-2 observations over Southern Europe and Northern Africa. GOME-2 NO_2 is smoother due to the coarser spatial resolution.
- In OMI data, shipping signals are apparent over the Mediterranean Sea and the Bay of Biscay. Shipping NO_2 can also be detected along the west and south side of the Iberian Peninsula and the Baltic Sea after high pass filtering (bottom panel in Figure 3.8). If NO_2 columns along the ship track are integrated, the shipping signal also can be identified between the Netherlands and Skagerrak (shown in Figure 3.9h).
- In GOME-2 data, the NO_2 plume across ship tracks is wider than for OMI, and the shipping signal is mixed with pollution from the continent, for example for the ship

lane around the Iberian Peninsula. Over the Mediterranean Sea, the shipping NO_2 from GOME-2 observation is higher than that from OMI observations.

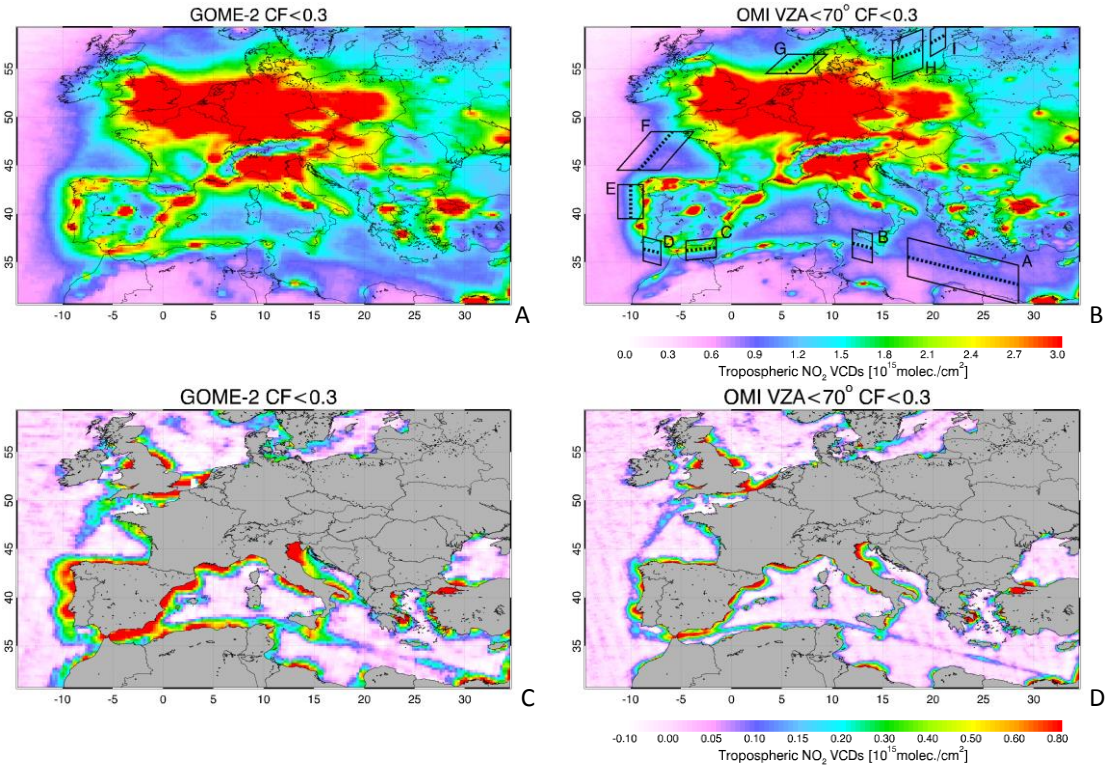

Figure 3.8 Muti-annual (Left: 2007-2010 for GOME-2 and right: 2005-2010 for OMI) mean tropospheric NO_2 from satellite observations over European waters (top panel), and results after high pass filtering (bottom panel). The nine selected areas (A-H) in the top right panel are visible ship lanes in the map or have been discussed in literatures.

3.5.2. Sensitivity study on shipping NO_2 detection

In order to investigate the effect of clouds, spatial resolution and wind field on the detection of shipping NO_2, a sensitivity study is presented based on the criteria of data selection described in Table 3.1. Analysis is based on a few selected shipping tracks (shown in Figure 3.8B), which are visible in the map or have been discussed in the literature (Beirle, et al., 2004; Richter et al., 2011; Vinken et al., 2014). In order to quantify the effect of each factor, data are integrated along the ship track (dashed line in Figure 3.8B, latitude for area E, F, G and longitude for the others) to create a cross section, and then a linear background fit is subtracted from the cross section. Results are shown in Figure 3.9.

Table 3.1: The criteria of data selection for statistics of NO_2 VCDs from satellite observations

Case	Instrument (Period)	Criteria of data selection
1	GOME-2 (2007-2010)	CF<30%, SA<0.3
2	OMI (2005-2010)	CF<30%, SA<0.3
3		All
4		CF<15%, SA<0.3
5		CF<30%, VZA<50°, SA<0.3
6		CF<30%, WS<5m/s, SA<0.3

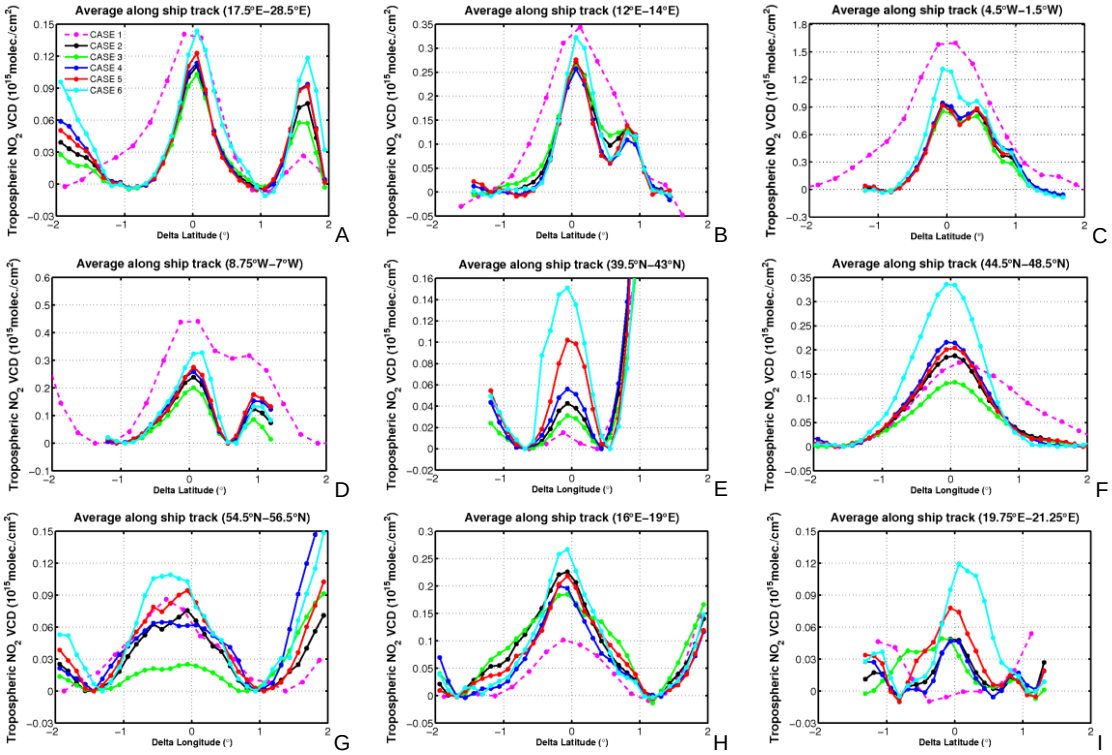

Figure 3.9 Along-ship-track averages of tropospheric NO_2 columns over the nine selected areas in Figure 3.8, as observed by GOME-2 and OMI. Data have been filtered with the criteria of Table 3.1, and a linear background fit was subtracted from the averages.

Spatial resolution

Atmospheric NO_2 hotspots are localized quite sharply due to the very short lifetime of boundary layer NOx. Therefore an improvement of the spatial resolution will improve the detection of the NO_2 signal from the narrow shipping tracks. At the same time, a better spatial resolution could also reduce cloud contamination.

The standard spatial resolution of the GOME-2 ground pixels is 80×40km^2, while OMI has a much better spatial resolution, varying from 13×24km^2 at nadir to 13×128km^2 at the outermost swath angles. Compared to OMI (case 2), shipping NO_2 from GOME-2 (case 1) is distributed over a much wider footprint for most of the areas, and the shipping signal is diluted due to the mixture of air pollution from the continent in several areas (such as E). Therefore, different emission sources cannot completely be separated in satellite observations when the ship track is close to the coast, especially for GOME-2. When the large pixels at the edge of the swath (VZA>50°, case 5) are excluded from OMI observations, the detection of the shipping signal can be further improved, in particular for ship lanes in south-west direction (areas E, G).

Cloud effects

As shown in Figure 3.10, more than 90% of all days offer a cloud fraction lower than 0.3 over the Mediterranean during summer. The fraction of clear-sky days decreases to 60-70% in winter. There are more cloudy days at high latitudes, in particular, less than 30% of all days present a cloud fraction lower than 0.3 in winter. If the threshold

of definition of the clear-sky day is taken to be 0.15 instead of 0.3, the number of clear days will decrease to 10%-20%.

Clouds not only shield the tropospheric gases below them, but also enhance the single and multiple scattering light paths from the sun to the cloud and back to the satellite, as compared to Rayleigh scattering light paths. Generally, for low clouds the enhancement of trace gas absorption in the gas layer above the cloud dominates while high clouds will lead to a reduction of tropospheric trace gas signals in satellite observations. The effect of clouds on trace gas retrievals also depends on the vertical distribution of the trace gas relative to the cloud position. Furthermore, the presence of clouds will affect the photochemical/heterogeneous reactions of nitrogen oxides in the atmosphere that change the lifetime and concentration of NO_2. Therefore, it is necessary to understand the effect of clouds on NO_2 measurements. Figure 3.11 displays the satellite observed NO_2 columns as a function of cloud fraction for the selected areas. Generally, NO_2 columns decrease with increasing cloud fraction with small seasonal variation. High NO_2 columns with large cloud fraction (>80%) are found over the North Sea area during winter, which is due to the occasional snow- and ice-cover related enhancements of the surface albedo, resulting in enhanced NO_2 signal in satellite observation. As surface albedo in the retrievals is from climatology, such effects are not corrected for in either NO_2 (AMF) or cloud retrieval (showing spurious enhanced cloud fraction).

As a result of the cloud effects on satellite NO_2 detection, the shipping NO_2 signal will be reduced when the analysis includes cloudy pixels (see cases 2-3 in Figure 3.9). The impact is small (<10%) over the Mediterranean Sea because of the small number (<20%) of cloud-covered scenes in this area. The shipping signal is significantly changed over the Bay of Biscay and North Sea areas, where the average NO_2 values including all cloud conditions are 30% to 70% smaller than the average values including only observations with a small cloud fraction. This result is consistent with the relation between observed NO_2 columns and cloud fraction. If the clear-sky condition is defined more stringently as cloud fraction below 0.15, there is a slight change in shipping NO_2 values (c.f. cases 2 and 4). On the other hand, the strict definition will exclude a relatively large number of observations in the analysis, especially at high latitudes where only a few days present small cloud fractions.

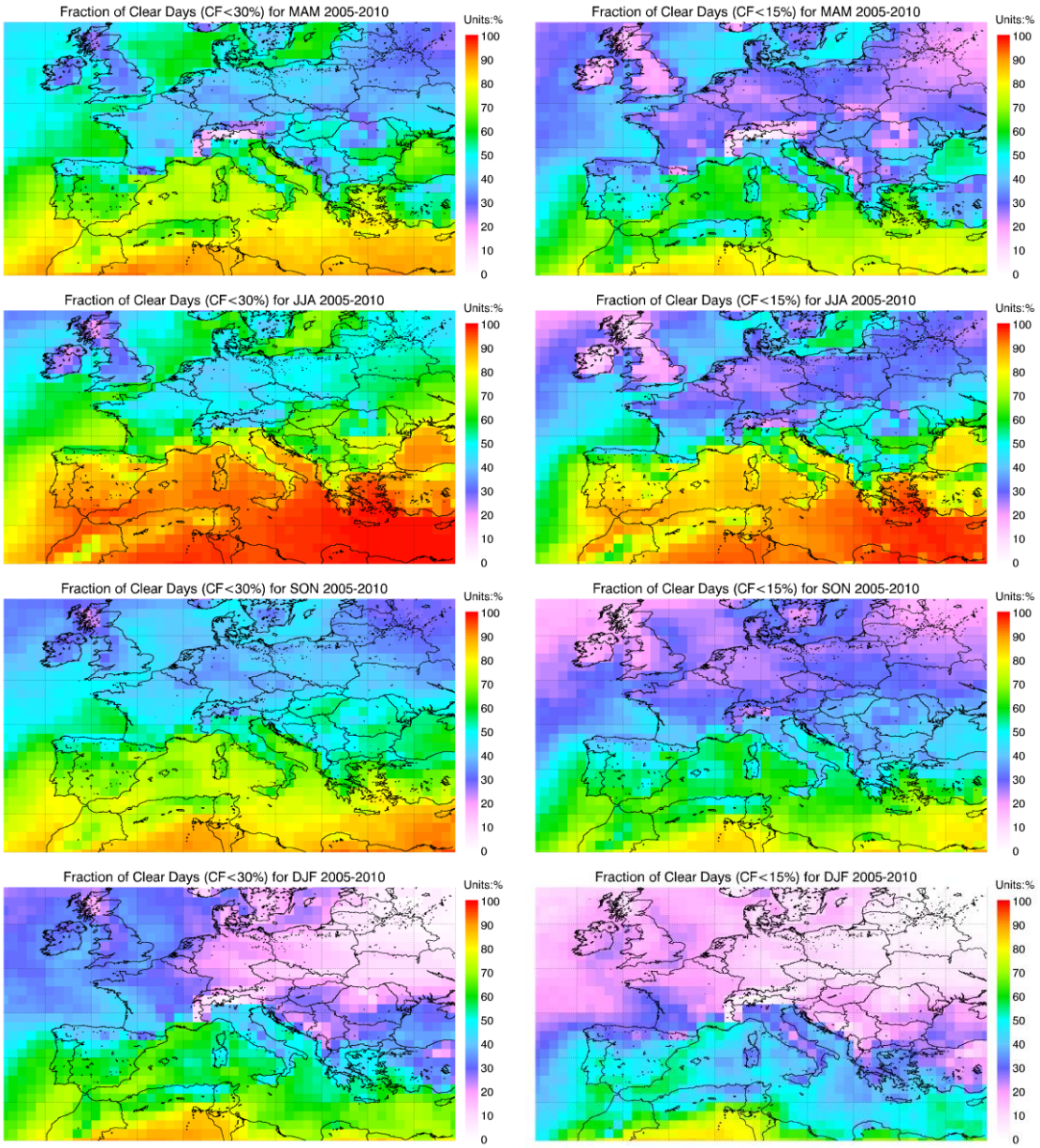

Figure 3.10 Seasonal clear-sky pixels over Europe for 2005-2010. Scenes are classified as "clear-sky" if the retrieved OMI effective cloud fraction is less than 30% (left panel) or less than 15% (right panel). Pixels having a surface albedo larger than 0.3 at 440nm are classified as cloudy scenes.

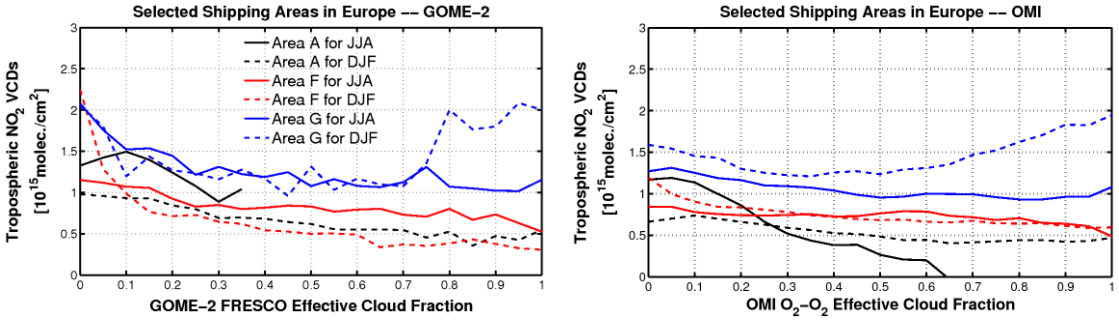

Figure 3.11 Distribution of seasonal median tropospheric NO_2 columns as a function of the effective cloud fraction for both GOME-2 and OMI observations over the selected European shipping areas (A, F, G) as shown in Figure 3.8B. Data analysis is based on the period 2007-2010 for GOME-2 and 2005-2010 for OMI observations. Satellite NO_2 columns were computed using AMFs without cloud correction (i.e. AMF are calculated for a completely clear scene). The effective cloud fractions are taken from the FRESCO+ and O_2-O_2 cloud schemes for GOME-2 and OMI, respectively. Measurements taken under sun glint geometry are excluded in the analysis.

Wind effects

Meteorological fields are derived from ECMWF ERA-Interim reanalysis data with a spatial resolution of 1°×1° and a frequency of 4 times a day (every 6 hours). Figure 3.12 shows seasonal averages of wind fields at the OMI overpass time (13:30 LT) linearly interpolated from ERA-Interim data for 2005-2010. At high latitudes, prevailing winds blow from west to east and are strongest in winter, while at low latitudes, they show a prominent seasonal variation. For shipping NO_2 detection, strong winds will lead to dispersion of the NO_2 plume emitted in the ship track, making its detection difficult.

Figure 3.13 counts the number of days with calm wind (defined as wind speed below a threshold of 5m/s) for different seasons. Results show more calm wind over continent than over ocean, and more windy conditions over high latitudes than over low latitudes. There are 50-60% of days with wind speed below 5m/s for most seasons over the Mediterranean, except in winter and the Eastern Mediterranean in summer; while there are always windy days at high latitudes (>75%), and only slightly less in summer.

The sensitivity study discussed above shows that the wind field (case 6) is the most important factor for the detection of shipping NO_2. Detected shipping NO_2 signals are larger by more than 20% for all the areas, especially for the ship lanes with south-north direction (signal increased by more than 50% for cases E, F, H), since the wind patterns over Europe are generally dominated by westerlies, and the shipping detection is more sensitive for wind directions across the ship track than along the ship lane direction. It should be noted that the lifetime of NOx also needs to be considered. For example, over the East Mediterranean (area A) during summer time, only a slight shift (0.1°-0.2° latitude) is found for the NO_2 cross section (Figure 3.18A) compared to the other seasons, since the lifetime of NO_2 is very short (a few hours) in this region during summer time. The effect of wind is expected to be more important for the shipping detection in winter and/or at high latitudes.

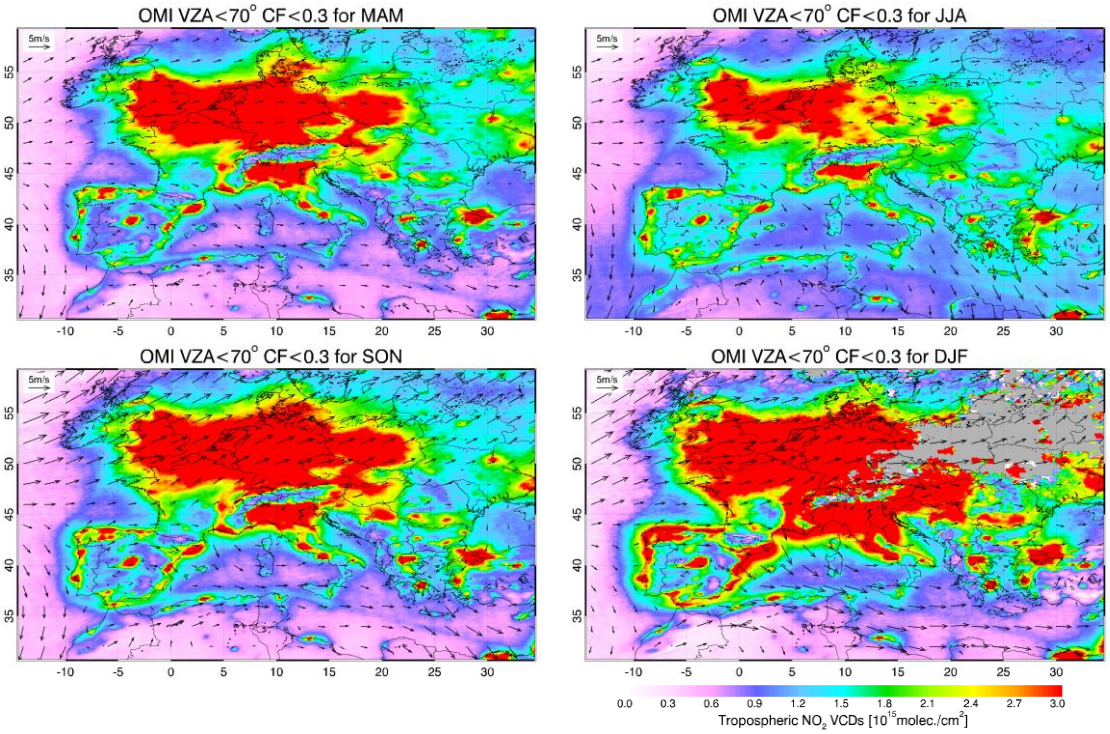

Figure 3.12 Seasonal averages of NO_2 VCDs from OMI and wind field from ECMWF reanalysis data over Europe for 2005-2010.

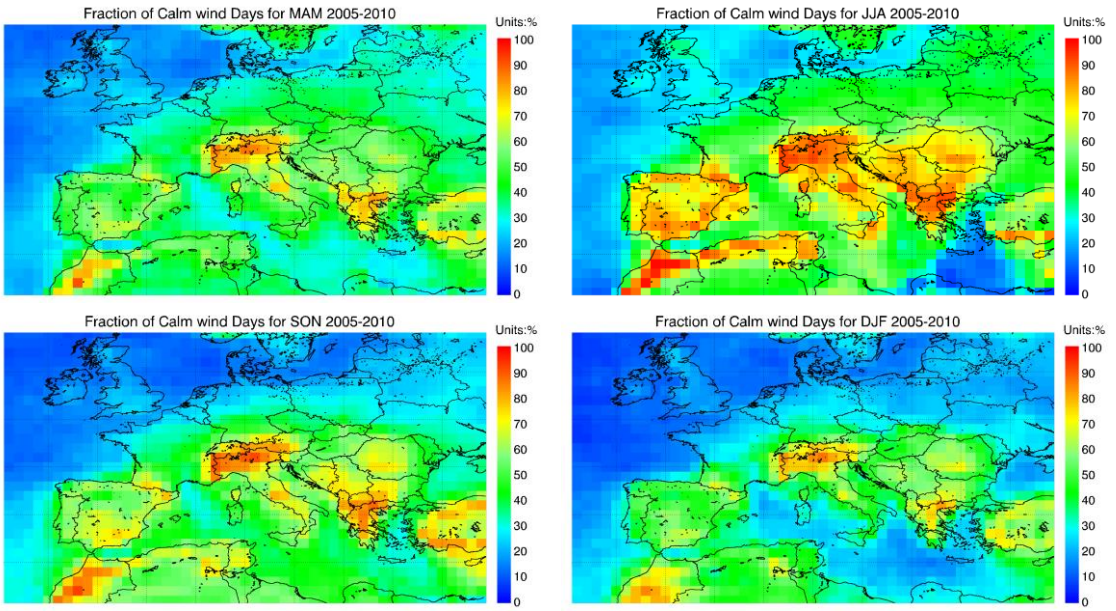

Figure 3.13 Percentage of calm days at OMI overpass time. The statistical analysis is based on 6-years (2005-2010) of ECMWF ERA-Interim reanalysis data, and calm wind is defined as situations with wind speed < 5m/s.

Sun glint observations

Sun glint occurs in imagery when the water surface and sun orientation is such that the sun light is directly reflected towards the sensor, which results in enhanced surface signals. Compared to low albedo values over the ocean, the observation over sun glint significantly increases the sensitivity of satellite observation to shipping NO_2. All instruments for NO_2 observation are affected by sun glint.

In order to understand the effect of sun glint on the NO_2 retrieval, we define the sun glint angle as the angle for which sun glint would occur if the ocean was a perfect mirror. The deviation from this angle $\Delta\Omega_{\mathrm{glint}}$ can be defined as:

$$\cos\Delta\Omega_{\mathrm{glint}} = \cos\theta\cos\theta_0 + \sin\theta\sin\theta_0\cos(\varphi - \varphi_0)$$

Where θ is the viewing zenith angle, θ_0 is the solar zenith angle, φ is the viewing azimuth angle, φ_0 is the solar azimuth angle. Geometrical sun glint occurs when the sun glint deviation angle is smaller than 18° (Wang et al., 2010).

As shown in Figure 3.14, sun glint mainly occurs in spring (February to April) and autumn (August to October) for polar-orbiting satellite observations over the tropical Indian Ocean, whereas the sun glint geometry is found only in summer over the southern part of European waters, namely the Mediterranean, and rarely at high latitudes (>45°). Averaged NO_2 maps (Figure 3.15) show a larger NO_2 peak along the ship track for the observations with sun glint geometry than for the other geometries for both the Indian Ocean and the Mediterranean areas, while no difference is observed over continents.

In order to quantify the effect of sun glint on NO_2, we integrated NO_2 along the ship track for three selected areas. The NO_2 peaks in the centre of the shipping lane increase by 35-50% for the Indian Ocean and by 50-100% for the Mediterranean. The discrepancy between GOME-2 and OMI is probably attributed to the effect of clouds. The NO_2 maps are averaged for pixels with cloud fraction lower than 30%. The sun glint effect will be significantly reduced in the presence of clouds, and its influence is not obvious when the cloud fraction is larger than 30%. There are more than 70% of completely clear days (CF<0.05) over the Mediterranean during summer time, while pixels with cloud fraction between 0.1 and 0.3 are more than 20% over Indian Ocean, accounting for approximately 50% of all pixels with CF below 0.3. Therefore, the average effect of sun glint on shipping NO_2 is larger over the Mediterranean than over the Indian Ocean.

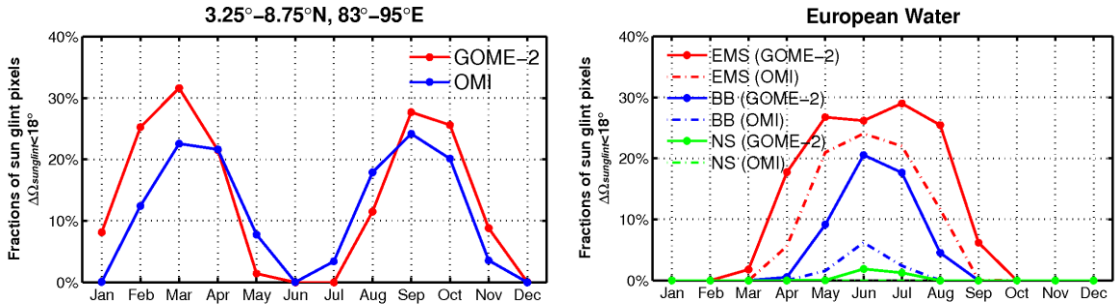

Figure 3.14: Fractions of satellite observations with sun glint geometry over the Indian Ocean (left) and three european water (right) areas.

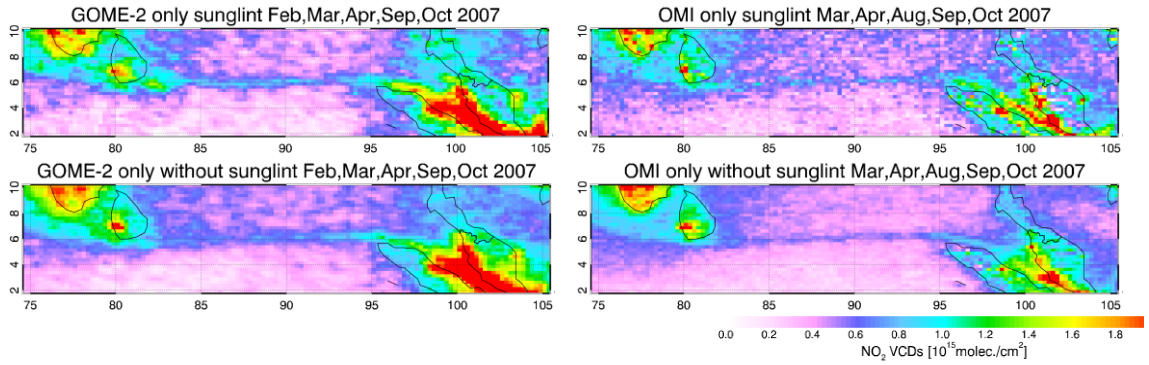

Figure 3.15 Comparison of tropospheric NO_2 columns for GOME-2 (left) and OMI (right) observations with sun glint geometry (upper panels) and observations excluding sun glint geometry over the IO area (lower panels) for five months of measurements when sun glint geometry often occurs (c.f. Figure 3.14). NO_2 retrievals use AMFs without cloud correction, and the data analysis is based on one year of satellite observations.

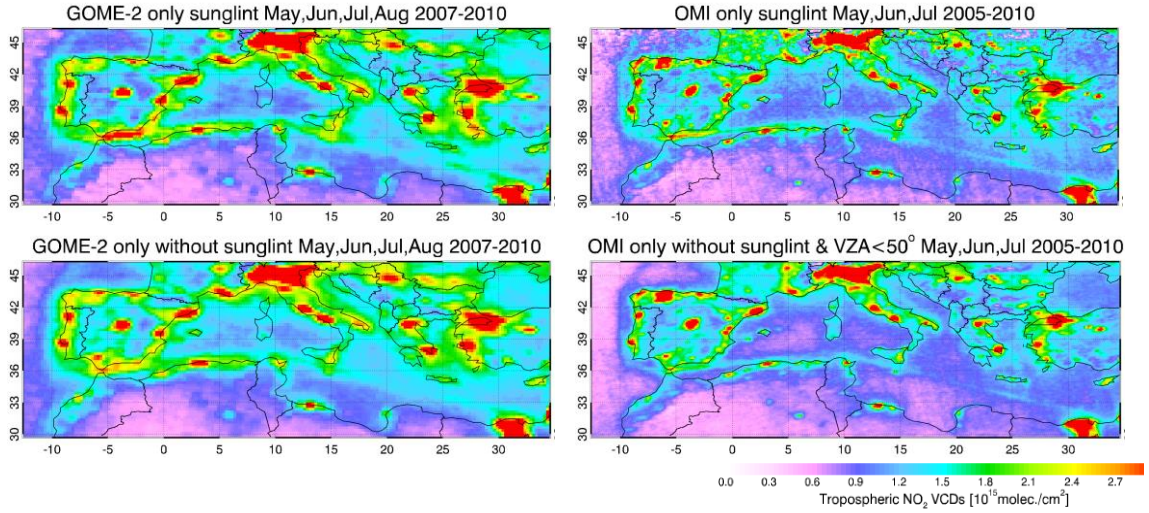

Figure 3.16 Same as 0, but for Mediterranean region. data analysis is based on multi-year records of satellite measurements (2007-2010 for GOME-2 and 2005-2010 for OMI). Larger pixels at the edge of the OMI swath are excluded.

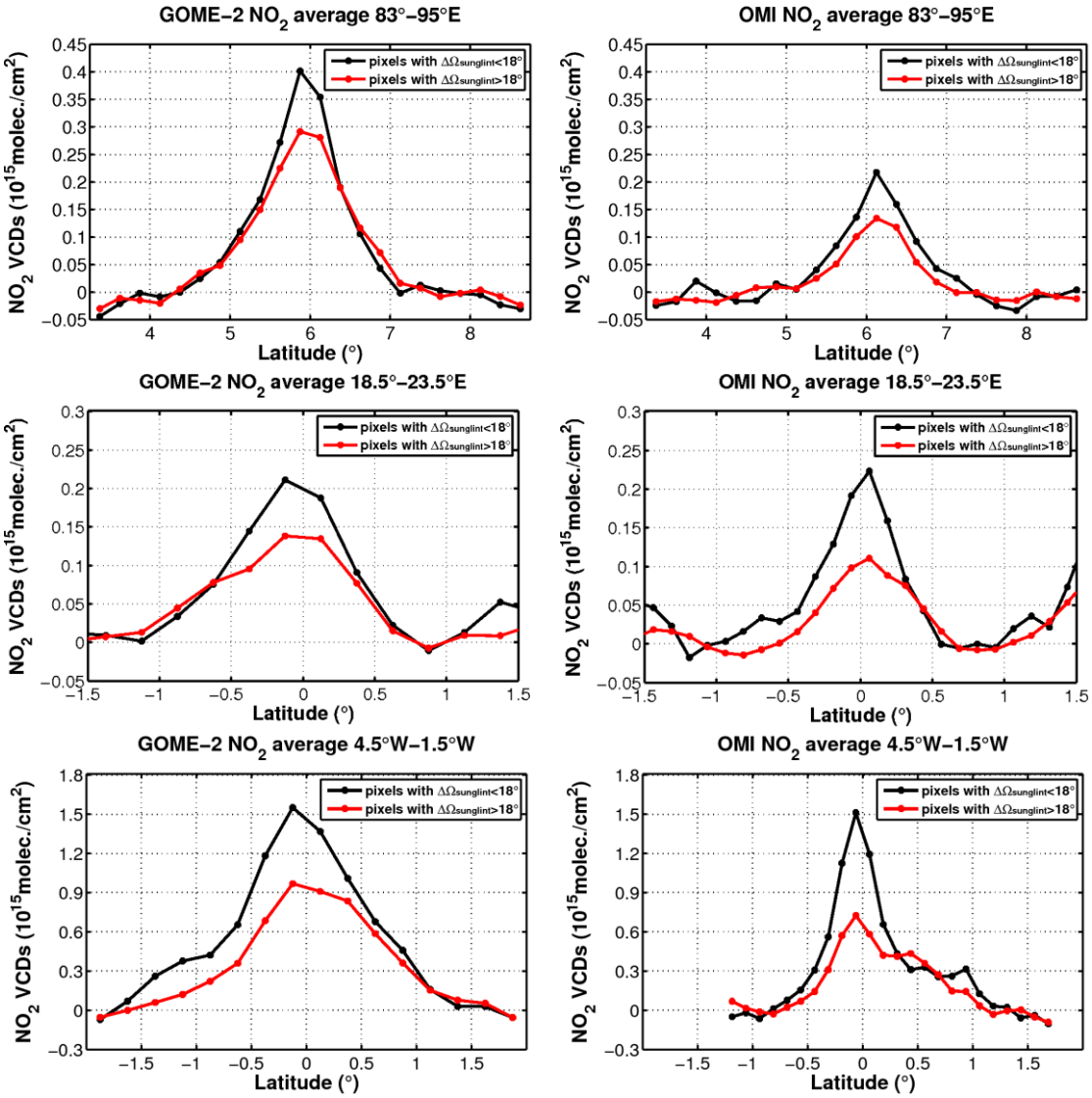

Figure 3.17 Comparison between along-ship-track averages of tropospheric NO_2 columns for GOME-2 (left) and OMI (right) observations under sun glint geometry (black) and excluding sung glint observations (red) over the Indian Ocean (upper panel) and two Mediterranean areas (middel panel: area A; bottom panel: area C in Figure 3.8). The area is averaged in longitude along the ship track, and a linear background fit is subtracted from the averages. Selection of satellite observations follows the same criteria as for Figure 3.15 and Figure 3.16.

3.5.3. Seasonal Variation

Seasonal averages of tropospheric NO_2 columns over Europe are shown in Figure 3.12. NO_2 data are obtained from OMI observations for 2005-2010, and pixels with cloud fraction above 0.3 are excluded. In order to assess the seasonal variation of the shipping signal, NO_2 cross sections are also created (Figure 3.18) by averaging the NO_2 along the selected ship tracks as shown in Figure 3.18B. Besides the selection criteria for cloud fraction, pixels with viewing angle larger than 50° are also excluded, but wind speed is not included in the data selection, because otherwise, a large number of valid pixels would be lost, and the signal-to-noise ratio would become too low in some cases.

The shipping signal shows little seasonal variation for most areas (area A-F), only winter (A, B, C) or autumn (D, E) signals show slightly larger differences compared to

other seasons. At high latitudes (for area G-I), the shipping signals are only apparent in summer (and spring for area G and H). In general, this variability of the shipping signal is probably not the result of emission changes since the change in ship traffic intensity is expected to be small over the year. the seasonal variation rather depends on the lifetime of NO_2 and on the dilution due to strong wind conditions.

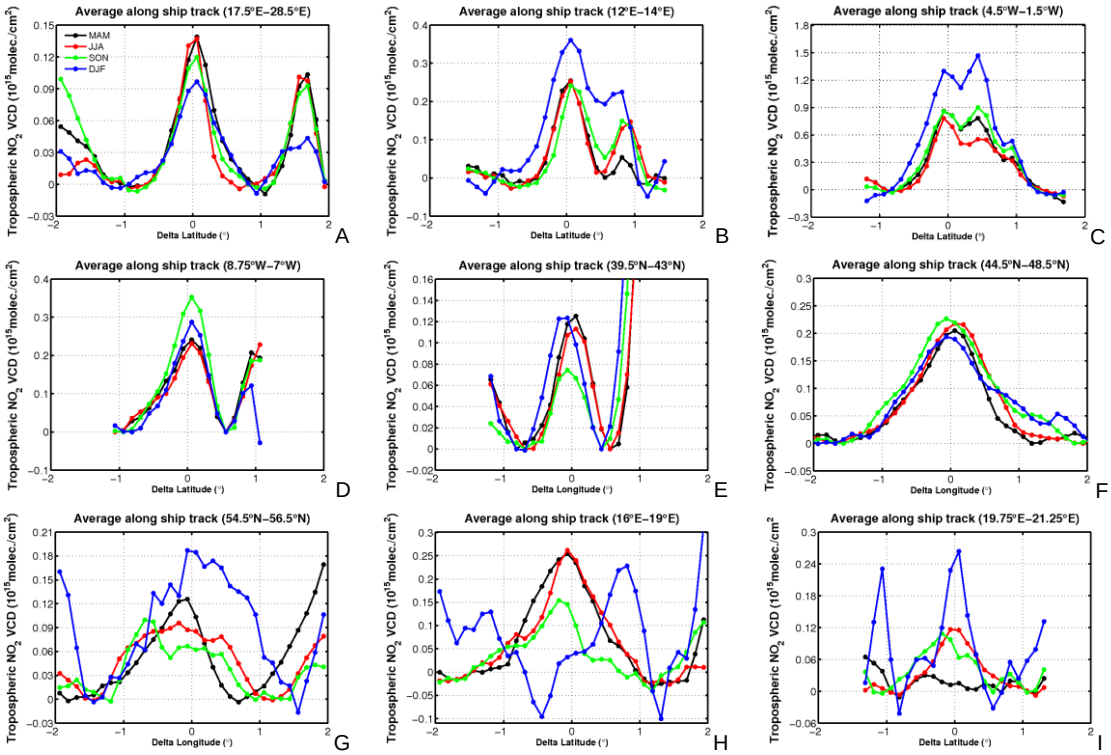

Figure 3.18 Seasonal averages of OMI NO_2 columns integrated along the shipping track over European waters shown in Figure 3.8. Only mesurements having effective cloud fractions below 0.3 and taken under near nadir geometries (VZA<50°) are used in the analysis (case 5 in Table 3.1). a linear background fit was subtracted from the averages.

3.6. Modelled NO_2 columns

Tropospheric NO_2 columns from CHIMERE model output over EMS, BB and NS is shown in Figure 3.19, together with long term average of NO_2 columns retrieved from OMI measurements. For this, only the model output for 12/14/13UTC over EMS/BB/NS was used, which is consistent with the OMI overpass time over these regions. According to the discussion above, OMI observations with VZA larger than 50° and effective cloud fraction above 0.3 are excluded to obtain clearer shipping signals and the criteria for favourable meteorological conditions (low wind speed) is also included in the analysis over NS to further increase the shipping signal in the NO_2 maps.

The Shipping lane in the EMS is clearly displayed in both the CHIMERE and OMI maps. For the BB, the ship lane from east of the Iberian Peninsula to Great Britain can be seen in CHIMERE and OMI data as well, but there is a shift in the position of the ship lane between the two maps, CHIMERE results lying 0.2°–0.3° to the west of the observations. Furthermore, there are two other ship lanes (east of the Iberian Peninsula to Saint-Nazaire and Great Britain to Santander) in modelled data which are not visible in satellite measurements. The shipping lane from Holland to Skagerrak strait displays a slightly enhanced NO_2 signal in OMI observations using

the strictest criteria for data selection, and this signal can be clearly seen in the averaged cross section through the ship track as shown in Figure 3.9G. This shipping lane is not visible in the modelled data, but there are two other ship tracks from the UK to Denmark/Norway which are visible.

It should be noted that the distribution of the seasonal averages of modelled NO_2 columns strongly depend on the emission inventory used as model input, because of the short NO_x lifetime. The Edgar database, which is used for the simulations shown here, includes the shipping emission from Holland to Skagerrak, but the intensity is much smaller than that of the other two tracks. We therefore conclude that the spatial pattern of the EDGAR ship emissions is not consistent with the NO_2 maps derived from OMI measurements in the North Sea area, and to a lesser degree also disagrees in the Bay of Biscay.

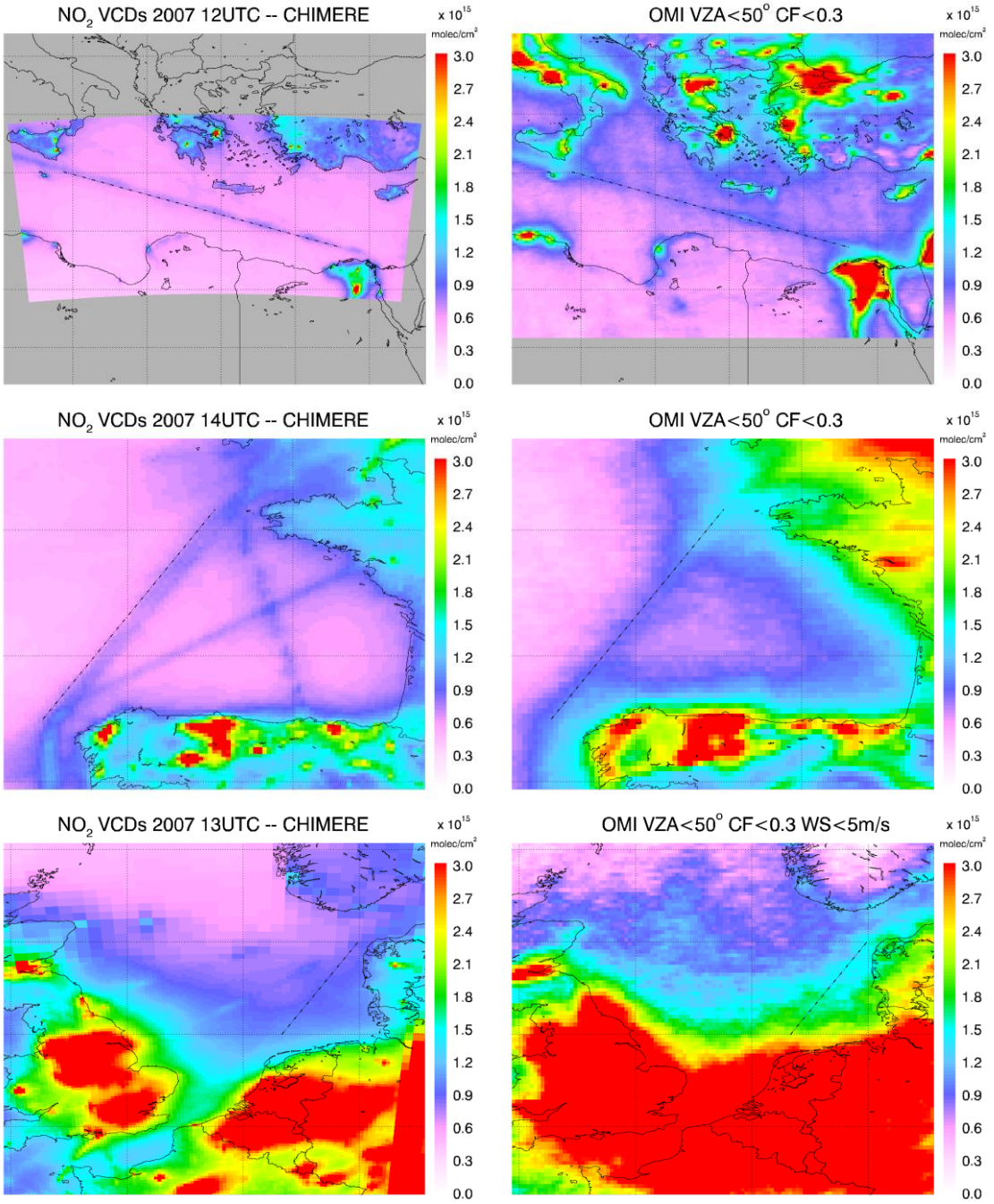

Figure 3.19 Annual average (2007) of modelled NO_2 columns (left panel) and long term average (2005-2010) of OMI NO_2 vertical columns (right panel) over EMS (top), BB (middle) and NS (bottom) (Jan-Apr-Jul-Oct average for BB and NS). The dash-dot lines represent the ship lanes detected from OMI measurements.

4. Shipping NO_2 identification

One important question for any satellite NO_2 product for ship emissions is the question of identification and attribution of the ship related signal in the NO_2 maps. Ideally, there is no other NOx source in the region of interest and satellite observed NO_2 columns can directly be assigned to ship emissions. However, in real data there are several complications:

Land based emission sources can impact the NO_2 columns over the ocean. As such sources are usually much larger than the ship emissions even a small contamination can have a significant impact on the estimated shipping signal. This was discussed in section 3.5 for the Strait of Gibraltar where contamination of the GOME-2 data is a problem. One approach to reduce the impact of continental pollution suggested by Vinken et al. (2014) is to limit the analysis to low wind speed situations. As shown in section 3.5.2, this in fact simplifies the detection of shipping NO_2 in some regions.

- As the result of outflow from the continents and from photochemistry in the atmosphere, there are gradients in the free tropospheric NO_2 fields which vary in space and time. Although the absolute magnitude of the tropospheric NO_2 background columns is small compared to most land based NO_2 hotspots, it is of a similar magnitude as the shipping signals. Therefore, some kind of background correction is needed in any NO_2 shipping product to remove the impact of the free troposphere.
- As the shipping signal is small, random noise and retrieval biases can be of a magnitude comparable to the signal. This also needs to be compensated, for example as part of a background correction.

  In previous work, different approaches have been taken to address this problem. In Richter et al. (2004) and Franke et al. (2009), the absolute tropospheric NO_2 columns are discussed for the Indian Ocean and the NO_2 background is estimated using measurements to the North and to the South of the shipping lane. This corresponds to the assumption of a background NO_2 field varying linearly with latitude and is based on manual identification of reference regions. In Beirle et al. (2004) as well as in Marbach et al. (2009), a spatial filtering was applied to separate the shipping signal from the background. This is an automatic procedure but leads to oscillation with negative NO_2 columns to the sides of the main shipping signal. In Vinken et al. (2014) and Ialongo et al. (2014), the shipping lanes were identified manually in the data, and the NO_2 was integrated along the ship track. The variation across the track was then corrected by subtracting a linear background, again based on manual selection. An alternative would be the use of an atmospheric model which can be run without including ship emissions. Ideally, the difference between measurements and model would then yield the shipping NO_2. However, the latter approach relies on excellent agreement between measurements and models which currently is not the case in the regions of interest.

  While for a known ship track manual selection of reference regions or background levels is feasible and probably a good approach, it would be preferable to have an automated and objective algorithm to extract the shipping signal. Spatial high pass filtering as proposed by Beirle et al. (2004) and for example used in has the potential to provide such data, and in the following, a sensitivity study on GOME-2 observations in the Indian Ocean region evaluates this approach.

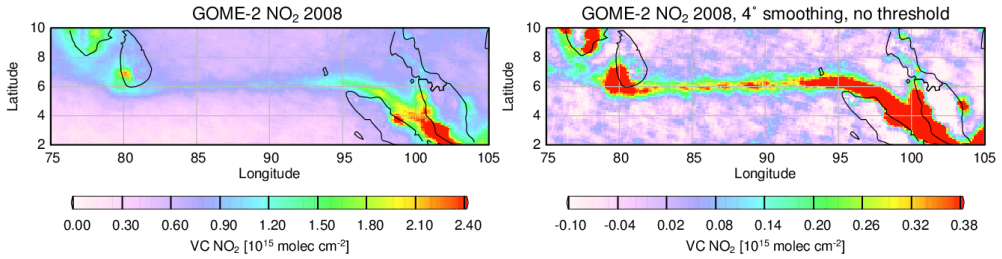

Figure 4.1: Annual mean GOME-2 NO_2 vertical columns over the Indian Ocean ship track. Only measurements having a cloud fraction <= 0.2 are included and a simple 400 m boundary layer AMF is applied. In the right figure, the same data is shown after high pass filtering using a smoothing over 4°x4°.

In Figure 4.1, the NO_2 field from one year (2008) of GOME-2 observations in the Indian Ocean is shown. Only data having cloud fractions smaller than 0.2 were used and a simple AMF for NO_2 in a 400m boundary layer over the ocean was applied. This AMF does not take into account the change in AMF across the ship track but this point is not important for the sensitivity study on filtering. As can be seen from the figure, there is a clear and spatially well localised NO_2 signal between the Southern tip of India and Indonesia which is only slightly tilted with respect to the 6°N latitude line. To the North and South of this track, NO_2 values are much lower with a North-South gradient of about $8x10^{14}$ molec cm^{-2} over the 8° latitude shown.
As the ship track has a sharp spatial structure over a smooth background, high pass filtering of the map in Figure 4.2a nicely isolates the shipping signal (see Figure 4.2b). There is however the problem that a choice needs to be made on the cut-off frequency to be used in the filter. Depending on this choice, the results vary considerably. This is illustrated in Figure 4.3 where the cross-section of the shipping plume derived from the data in Figure 4.3 is shown for different filter constants. The filtering here is performed by smoothing the NO_2 field with a sliding boxcar and subtracting the smoothed field from the original to extract the high spatial frequency part. Clearly, changing the smoothing from 0.5° (+/- 0.25°) to 1°, 2°, 4° and 8° successively increases the apparent shipping NO_2 signal. In addition, larger negative side lobes appear as the smoothing range increases.

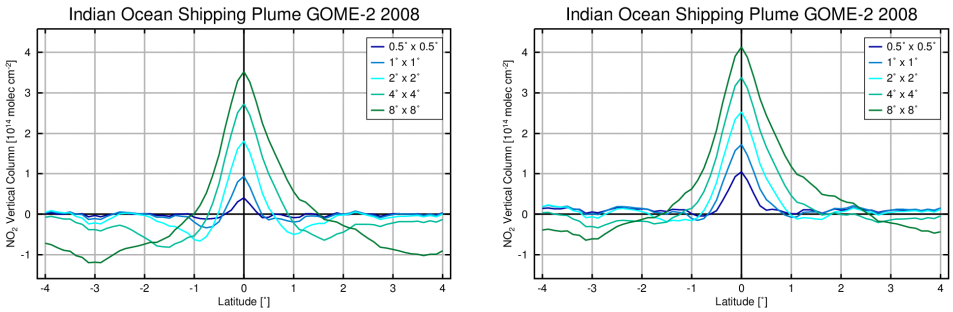

Figure 4.2: Cross sections through the shipping plume in the Indian Ocean integrated along longitude from 82°E to 92°E. Different filtering cut-offs have been used as indicated in the legend. In the left panel, all data have been used while in the right panel, a threshold of $1x10^{13}$ molec cm^{-2} has been applied after the first iteration and the filtering repeated without these values.

As already mentioned in section 3.5.1, the negative values can be much reduced by applying an iterative filtering procedure in which a first high frequency residual is computed as described before, and from this a tentative ship track is identified by selecting NO_2 values above a threshold. As these values are not part of the background and therefore should not be included in the smoothing, they are then

masked out and filled with interpolated values in the original data before a second smooth background is computed. This procedure can in principle be further iterated, but already the first iteration leads to a strong suppression of negative values as shown in Figure 4.3.

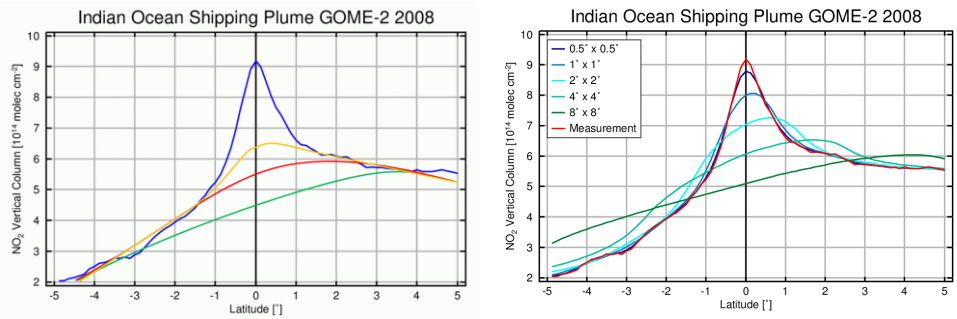

Figure 4.3: Illustration of the background problem for the shipping plume in the Indian Ocean. In the left panel, the measured (unfiltered) NO_2 data integrated along the ship track is shown together with some plausible approximations for the background NO_2 levels sketched by hand. In the right panel, the measurement is smoothed with a sliding boxcar over different latitude ranges approximating the background fields used in the filtering for Figure 4.2

However, the basic problem remains that the different filter choices lead to very different plume shapes and magnitudes, and would result in quite different estimates for shipping NOx emissions. The reason for this problem is the difficulty in defining the background levels. This is illustrated in Figure 4.3a, where the original cross-section of the plume is shown together with three manually added estimates of the background levels. Each of them would lead to a different shipping signal, and without additional information, it is not clear which of them is the most realistic one. For comparison, the smoothed cross-sections are also shown in Figure 4.3b which is not identical to the spatial filtering applied but illustrates the effect.

No general solution can be found for this problem, and at this point, any maps of shipping NO_2 created by high pass filtering depend on the subjective choice of the filter cut-off. If very good agreement is found between model and measurements, model values could be used at least in a relative way (by scaling them to measurement values over a clean region), but this introduces other uncertainties. Transfer of the spatial gradient from a clean region at the same latitude but other longitude (comparable to the reference sector method) could also be tried, but in case of the Indian Ocean leads to clear artefacts as it is dominated by outflow from the Indian continent. The only clear recommendation which can be made here is that any comparison of shipping NO_2 values derived with spatial filtering to model data has to apply exactly the same filtering procedure to the model data to minimise potential biases.

5. Conversion of NO_2 columns to NOx emissions

The quantity of interest in the observations of shipping emissions is the NOx emissions from ships which is related to the satellite observed NO_2 columns but not the same quantity. Ideally, one would like to determine NOx emissions per ship, but clearly this is out of reach for current space instruments for reasons of spatial resolution. Even with a perfect instrument having a very fine spatial resolution, this would be a challenge as in busy shipping lanes, it is not trivial to separate between emissions from individual ships and between the NO_2 background and the NO_2 from a single ship. For local campaigns, such measurements were done by aircraft either on isolated ships or at favourable wind directions.

The link between emissions of NOx and NO_2 columns is provided by chemistry and transport of NOx in the atmosphere. While emissions provide a continuous inflow of NOx at the lowest layers of the atmosphere, chemical reactions create an equilibrium between NO and NO_2 in each atmospheric layer and lead to NOx loss from the atmosphere, for example by formation of HNO_3 and subsequent washout. At the same time, some NOx is advected into a given volume from the outside while another amount of NOx is moved out of the volume, both vertically and horizontally. These complex and non-linear processes are simulated in CTMs and any formal inversion NO_2 columns observed by satellite to NOx emissions at the surface need to take into account the complex interplay of chemistry, transport and vertical integration. As such an inversion is a slow process, simplifications are needed for a fast estimation of NOx emissions from satellite observed NO_2 columns.

Such a simplified scheme has been proposed by Martin et al., 2003 and later been refined by Lamsal et al., 2011 in that for each grid cell of a model simulation, a ratio was determined between the NOx emission in the model and the NO_2 column in the model. In first (linear) approximation, a change in NOx emissions by 10% will lead to a corresponding change of NO_2 column by 10%. With this simplification, satellite observed NO_2 columns can be directly converted into NOx emissions.

Clearly, this approach is based on a number of assumptions which need to be kept in mind:

- The modelled NO_2 column must be in good agreement with the observed column to make this a valid approach
- The region considered must be large enough that transport in and out of the area can be neglected
- The changes of NOx emission must be small enough to warrant linearisation of the NOx chemistry
- The change in NO_2 profile must be small enough to allow neglecting changes in NO_2 AMF due to NOx emission changes.

Here, we take this simplified approach by using ratios between NO_2 columns and NOx emissions from the CHIMERE model. As test region, we select the busiest and clearest shipping lane in the Indian Ocean, and integrate over the entire shipping lane to reduce the impact of measurement noise and spatial mismatches between the real shipping lane position and the emission inventory. A full inversion approach considering non-linearities in both chemistry and AMF has recently been described by Vinken et al., 2014.

In Figure 5.1, as a first test the NO_2 columns integrated over the cross-section of the Indian Ocean plume have been plotted for all model days. To isolate the ship emissions, a simple linear background has been removed from the model signal. There is an obvious seasonality with higher values in northern hemispheric winter but also a large day to day variation in some months. The latter results from changes in meteorology which largely affect the lifetime of NO_2 and also can remove some of the

NO_2 out of the integration area. This variability is an intrinsic limitation to the method proposed here, and in order to reduce the impact of meteorology, is seems advisable to use monthly averages as in previous studies. These monthly values are also shown in In Figure 5.1,

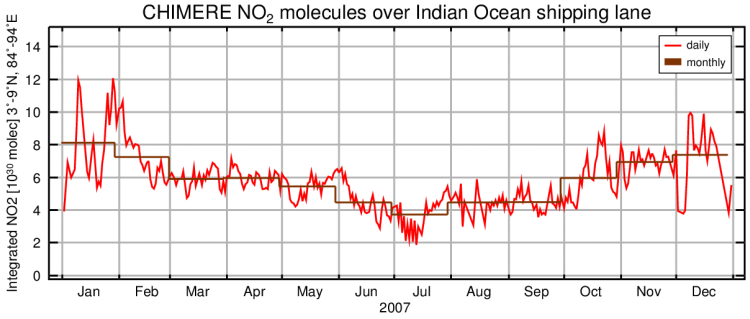

Figure 5.1: integrated amount of NO_2 in the Indian Ocean shipping lane as modelled by CHIMERE for approximately the GOME-2 overpass time. Units are molecules NO_2 and depend on the exact area selected (3°-9°N, 84°-94°E). A linear background is subtracted to isolate the shipping signal.

The monthly integrated NO_2 amounts can be compared to the ship emissions used in the model run in the same area. Although emissions in CHIMERE depend on time of the day and on day type (weekday, Saturday, Sunday), ship emissions do not show variability with these parameters. However, they show some variation with month for unknown reasons, possibly using information from ship density.

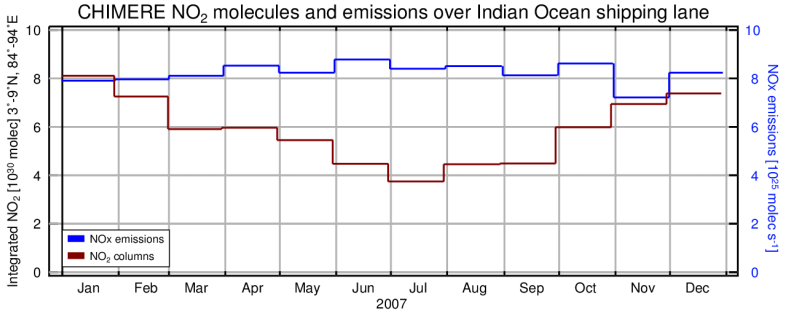

Figure 5.2: Comparison between integrated NO2 amount from CHIMERE and the NOx emissions used in the model run for the Indian Ocean region (see Figure 5.1).

As can be seen from Figure 5.2, variations in emissions are small compared to the variation in NO_2 columns which are driven by changes in photochemistry and meteorology. For a simple conversion factor between columns and emissions, one would just compute the ratio between emissions and column in the model $\tau = E_{NO2}/C_{NO2}$ and multiply the measured column with this factor. Such a simple approach is however based on very good agreement between model and measurement for a scenario where the emissions are known. Unfortunately, no such data set is available. However, one can compare the modelled and measured NO_2 columns as already done in section 3.4. Here, a slightly different view of the same data is shown in **Error! Reference source not found.** by comparing the integrated olumn in the Indian Ocean area between model (2007) and GOME-2 (2007 – 2012).

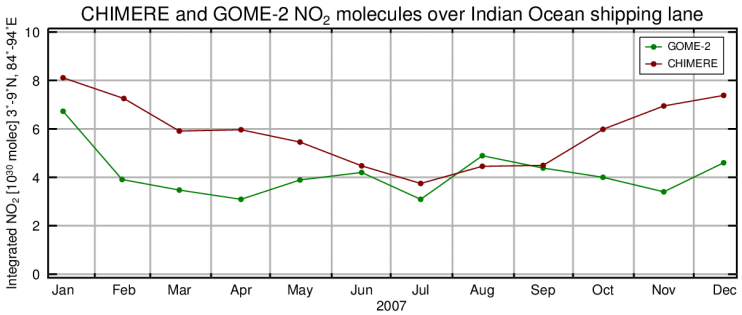

Figure 5.3: Comparison of integrated NO_2 amounts in the Indian Ocean region (see Figure 5.1) as modelled by CHIMERE (brown, 2007 only) and retrieved from GOME-2 observations (green).

Clearly, the seasonality in the model data is much more pronounced than in the measurements, a fact already highlighted in section 3.4. While in summer the agreement between CHIMERE and GOME-2 is close, this is not the case in winter. Thus, application of the τ factor to the ratio (see Figure 5.4) would result in a strong seasonality of the derived shipping emissions, which is not in agreement with expectations. It is therefore concluded that at least this CHIMERE model run is not sufficiently close to reality to be used in such a scheme.

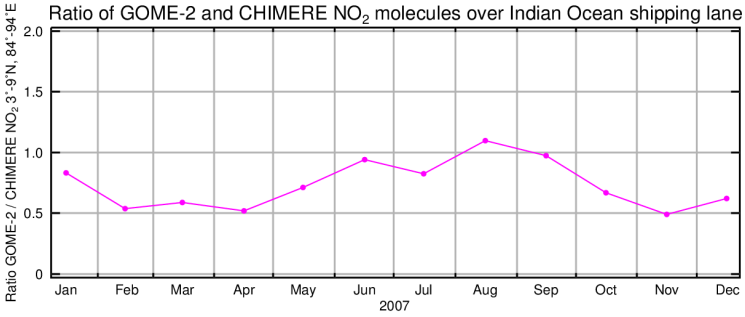

Figure 5.4: Ratio of the GOME-2 observed and the CHIMERE modelled total NO_2 molecules in the Indian Ocean region for 2007 (see Error! Reference source not found.**). ccording to the simple scaling approach, this would be the scaling factor for the ship emissions in the Indian Ocean.**

Different points could contribute to this mismatch between model and observations:

- A mismatch in emissions (this would be the ideal case for which the concept of emission estimate would work)
- A mismatch in the AMF used in the retrieval. However, here we used the GOME-2 data with CHIMERE AMF (see section **Error! Reference source ot found.**) so this source of inconsistency can be excluded
- An unrealistic seasonality in the NOx lifetime of the model, either from chemistry or from sinks linked to meteorology
- An unrealistic seasonality in NO_2 columns resulting from changes in meteorology through the year.

Unfortunately, at this point it cannot be decided what the cause of this mismatch in modelled and satellite observed NO_2 columns is.

It is interesting to note that this problem is not limited to the approach followed here. Also the much more complex approach taken by Vinken et al., 2014 relies on comparison of modelled and measured NO_2 columns. Any inaccuracy of the model would be interpreted as deficiency in the emissions and result in an according change of these. In fact, differences between OMI and GEOS-chem NO_2 columns over

European waters are of a similar magnitude in that study as those shown in **Error! eference source not found.** for the Indian Ocean, resulting in the need for significant adaptations of emission strengths. Whether or not the GEOS-chem run produced a more realistic seasonal variation of NO_2 in shipping lanes than the CHIMERE results used here is not clear as the only comparison of seasonalities shown in Vinken et al. (2014) is integrated over all of Europe.

6. Conclusions

In this report, the potential of satellite observed tropospheric NO_2 columns to be used for the estimation of shipping NOx emissions has been evaluated. First, in a series of sensitivity studies, a number of approaches have been evaluated to improve the detection of NO_2 signal from ships. The main results are that

- The use of a **larger fitting window** in the NO_2 retrieval reduces the noise of the shipping NO_2 signal
- The noise of the data can further be reduced by applying an **improved gridding algorithm** based on a fine sub-grid sampling and subsequent averaging on the final grid. By careful adaptation of the final grid size to the geophysical dimensions of the NO_2 ship track an optimum in detectability and low noise can be obtained.
- **Cloud contamination** is a problem for any tropospheric NO_2 product, and this is also the case for shipping signals. Depending on region, limitation to cloud free observations increases the observed shipping signal albeit at a loss of the number of satellite measurements included in the averages. The effect is particularly pronounced in the Bay of Biscay region.
- Observations taken under **sun-glint** geometry provide higher sensitivity to the boundary layer NO_2. Consequently, the shipping signal is larger in GOME-2 and OMI data if only sun-glint geometries are used for the averages. However, the number of these observations is limited spatially and temporally in European waters, and cloud contamination imposes additional limitations.
- Limitation to **low wind speeds** increases the observed shipping signal in some regions as dilution by wind as well as contamination by NO_2 from land-based sources is reduced. However, in particular in the North Sea region, the number of calm situations is small, reducing the data base for averaging and therefore the signal to noise ration of the resulting averages.
- **Spatial filtering** can be applied to detect and quantify shipping NO_2 in ocean regions in an automatic and objective way. In order to improve the detection and to reduce occurrences of negative side lobes, an iterative approach is needed in which detected shipping regions are removed from the data set used for background determination applying a threshold technique. As in all filtering techniques, the choice of cut-off value is critical and using too little smoothing in the filter will artificially reduce the shipping signal. More work is needed to determine optimal choices of this parameter for all shipping regions.
- Conversion of NO_2 columns to **NOx emissions** relies on accurate modelling of atmospheric NO_2 over shipping lanes. While the agreement between CHIMERE modelled columns produced in this study and satellite data is reasonable, differences in the seasonality and spatial distribution are a problem for the conversion of NO_2 columns to NOx emission strengths.

References

Beirle, S., Platt, U, von Glasow, R., Wenig, M., Wagner, T.: Estimate of nitrogen oxide emissions from shipping by satellite, *Geophys. Res. Lett.*, 31, L18102, doi:10.1029/2004GL020312, 2004.

de Ruyter de Wildt, M., Eskes, H., and Boersma, K. F.: The global economic cycle and satellite-derived NO2 trends over shipping lanes*, Geophys. Res. Lett.,* 39, L01802, doi: 10.1029/2011GL049541, 2012.

Franke, K., Richter, A., Bovensmann, H., Eyring, V., Jöckel, P., and J. P. Burrows, Ship emitted NO2 in the Indian Ocean: comparison of model results with satellite data, *Atmos. Chem. Phys.*, **9**, 7289-7301, 2009.

Heckel, A., Kim, S.-W., Frost, G. J., Richter, A., Trainer, M., and Burrows, J. P.: Influence of low spatial resolution a priori data on tropospheric NO2 satellite retrievals, *Atmos. Meas. Tech.*, **4**, 1805-1820, doi:10.5194/amt-4-1805-2011, 2011.

Ialongo, I., Hakkarainen, J., Hyttinen, N., Jalkanen, J.-P., Johansson, L., Boersma, K. F., Krotkov, N., and Tamminen, J.: Characterization of OMI tropospheric NO2 over the Baltic Sea region, *Atmos. Chem. Phys.*, 14, 7795-7805, doi:10.5194/acp-14-7795-2014, 2014.

Irie, H., Boersma, K. F., Kanaya, Y., Takashima, H., Pan, X., and Wang, Z. F.: Quantitative bias estimates for tropospheric NO2 columns retrieved from SCIAMACHY, OMI, and GOME-2 using a common standard for East Asia, Atmos. Meas. Tech., 5, 2403–2411, doi:10.5194/amt-5-2403-2012, 2012.

Kleipool, Q. L., Dobber, M. R., de Haan, J. F., and Levelt, P. F.: Earth surface reflectance climatology from 3 year of OMI data, *J. Geophys. Res.*, 113, D18308, doi:10.1029/2008JD010290, 2008.

Lamsal, L. N., R. V. Martin, A. Padmanabhan, A. van Donkelaar, Q. Zhang, C. E. Sioris, K. Chance, T. P. Kurosu, and M. J. Newchurch, Application of satellite observations for timely updates to global anthropogenic NOx emission inventories, Geophys. Res. Lett., 38, L05810, doi:10.1029/2010GL046476, 2011.

Lin, J.-T., Martin, R. V., Boersma, K. F., Sneep, M., Stammes, P., Spurr, R., Wang, P., Van Roozendael, M., Clémer, K., and Irie, H.: Retrieving tropospheric nitrogen dioxide from the Ozone Monitoring Instrument: effects of aerosols, surface reflectance anisotropy, and vertical profile of nitrogen dioxide, Atmos. Chem. Phys., 14, 1441–1461, doi:10.5194/acp-14-1441-2014, 2014.

Ma, J. Z., Beirle, S., Jin, J. L., Shaiganfar, R., Yan, P., and Wagner, T.: Tropospheric NO2 vertical column densities over Beijing: results of the first three years of ground-based MAX-DOAS measurements (2008–2011) and satellite validation, Atmos. Chem. Phys., 13, 1547–1567, doi:10.5194/acp-13-1547-2013, 2013.

Marbach, T., Beirle, S., Platt, U., Hoor, P., Wittrock, F., Richter, A., Vrekoussis, M., Grzegorski, M., Burrows, J. P., and Wagner, T., Satellite measurements of formaldehyde from shipping emissions, Atmos. Chem. Phys., 9, 8223-8234, 2009

Martin, R. V., D. J. Jacob, K. Chance, T. P. Kurosu, P. I. Palmer, and M. J. Evans, Global inventory of nitrogen dioxide emissions constrained by space-based observations of NO2 columns, J. Geophys. Res., 108(D17), 4537, doi:10.1029/2003JD003453, 2003.

Marmer, E., Dentener, F., Aardenne, J. v., Cavalli, F., Vignati, E., Velchev, K., Hjorth, J., Boersma, F., Vinken, G., Mihalopoulos, N., and Raes, F.: What can we learn about ship emission inventories from measurements of air pollutants

over the Mediterranean Sea?, *Atmos. Chem. Phys.*, **9**, 6815-6831, doi:10.5194/acp-9-6815-2009, 2009.

Richter, V. Eyring, J. P. Burrows, H. Bovensmann, A. Lauer, B. Sierk, and P. J. Crutzen, Satellite Measurements of NO_2 from International Shipping Emissions, *Geophys. Res. Lett.*, **31**, L23110, doi:10.1029/2004GL020822. 2004.

Richter, A., Begoin, M., Hilboll, A., Burrows, J. P.: An improved NO_2 retrieval for the GOME-2 satellite instrument, *Atmos. Meas. Tech.*, 4, 1147-1159, 2011, *www.atmos-meas-tech.net/4/1147/2011/*www.atmos-meas-tech.net/4/1147/2011/, doi:10.5194/amt-4-1147-2011.

Stammes, P., Sneep, M., de Haan, J. F., Veefkind, J. P., Wang, P., Levelt, P. F.: Effective cloud fractions from the Ozone Monitoring Instrument: Theoretical framework and validation, *J. Geophys. Res.*, 113, D16S38, doi:10.1029/2007JD008820, 2008.

Theys, N., I. De Smedt, J. van Gent, T. Danckaert, T. Wang, F. Hendrick, T. Stavrakou, S. Bauduin, L. Clarisse, C. Li, N. Krotkov, H. Yu, H. Brenot, and M. Van Roozendael, Sulphur dioxide vertical column DOAS retrievals from the Ozone Monitoring Instrument: global observations and comparison to ground-based and satellite data, submitted to *J. Geophys. Res.* (2014).

Van der A, R. J., H. J. Eskes, K. F. Boersma, T. P. C. van Noije, M. Van Roozendael, I. De Smedt, D. H. M. U. Peters, and E. W. Meijer, Trends, seasonal variability and dominant NOx source derived from a ten year record of NO_2 measured from space, J. Geophys. Res., 113(D4), D04302, doi:10.1029/2007JD009021, 2008.

Veefkind, J. P., Aben, I., Mcmullan, K., Forster, H., de Vries, J., Otter, G., Claas, J., Eskes, H. J., de Haan, J. F., Kleipool, Q., van Weele, M., Hasekamp, O., Hoogeveen, R., Landgraf, J., Snel, R., Tol, P., Ingman, P., Voors, R., Kruizinga, B., Vinck, R., Visser, H., Levelt, P. F.: TROPOMI on the ESA Sentinel-5 Precursor: A GMES mission for global observations of the atmospheric composition for climate, air quality and ozone layer applications. *Remote Sensing of Environment*, doi:10.1016/jrse2011.09.27, 2012.

Vinken, G. C. M., Boersma, K. F., van Donkelaar, A., and Zhang, L.: Constraints on ship NO_x emissions in Europe using GEOS-Chem and OMI satellite NO_2 observations, Atmos. Chem. Phys., 14, 1353-1369, doi:10.5194/acp-14-1353-2014, 2014.Wang, P., Tuinder, O., Stammes, P.: Cloud retrieval algorithm for GOME-2: FRESCO+, EUM/CO/09/4600000655/RM, 2010.

Yu, H., Van Roozendael, M., Wang, P., De Smedt, I., van Gent, J., van der A, R., Boersma, F., Valks, P., Richter, A., Stavrakou, T., and Müller, J.-F.: Intercomparison of tropospheric NO_2 retrievals from the OMI and GOME-2 sensors over China, poster presentation at Living Planet Symposium Edinburgh, Edinburgh, 2013.